

University of Nebraska - Lincoln

DigitalCommons@University of Nebraska - Lincoln

Mechanical (and Materials) Engineering --
Dissertations, Theses, and Student Research

Mechanical & Materials Engineering,
Department of

Spring 2-4-2011

Design and Analysis of Blast Induced Traumatic Brain Injury Mechanism Using a Surrogate Headform: Instrumentation and Outcomes

Eyitejumade A. Sogbesan

University of Nebraska-Lincoln, eyitejumade.sogbesan@huskers.unl.edu

Follow this and additional works at: <https://digitalcommons.unl.edu/mechengdiss>



Part of the [Mechanical Engineering Commons](#)

Sogbesan, Eyitejumade A., "Design and Analysis of Blast Induced Traumatic Brain Injury Mechanism Using a Surrogate Headform: Instrumentation and Outcomes" (2011). *Mechanical (and Materials) Engineering -- Dissertations, Theses, and Student Research*. 18.
<https://digitalcommons.unl.edu/mechengdiss/18>

This Article is brought to you for free and open access by the Mechanical & Materials Engineering, Department of at DigitalCommons@University of Nebraska - Lincoln. It has been accepted for inclusion in Mechanical (and Materials) Engineering -- Dissertations, Theses, and Student Research by an authorized administrator of DigitalCommons@University of Nebraska - Lincoln.

Design and Analysis of Blast Induced Traumatic Brain Injury Mechanism Using a
Surrogate Headform: Instrumentation and Outcomes

By

Eyitejumade A. Sogbesan

A THESIS

Presented to the Faculty of

The Graduate College at the University of Nebraska

In Partial Fulfillment of Requirements

For the Degree of Master of Science

Major: Mechanical Engineering

Under the Supervision of Professor Carl A. Nelson

Lincoln, Nebraska

May, 2011

Design and Analysis of Blast Induced Traumatic Brain Injury Mechanism Using a
Surrogate Headform: Instrumentation and Outcomes

Eyitejumade A. Sogbesan, M.S.

University of Nebraska, 2011

Advisor: Carl A. Nelson

Brain injury cases in military personnel exposed to improvised explosive devices (IED) in combat have been on the rise. In Iraq and Afghanistan improved helmets and body armor are not enough protection against blast wave threats. The United States military are sponsoring researchers and scientists around the globe to find the associations between pressure waves and traumatic brain injury (TBI).

Lack of accurate data and blast wave exposure information in returning soldiers has slowed the innovation needed to effectively diagnose TBI and other related brain injury as a result of pressure waves. More detailed data will be required to gain a better understanding of the mechanisms responsible for blast-induced TBI and to design and develop a more effective head protection system.

Understanding the impacts of blast wave in the brain could lead to understanding the best form of protection the head needs in such a scenario. Developing an accurate model suitable for the simulation of the mechanical behavior of the human brain under blast loading conditions could lead to significant advances.

This thesis introduces a research study on blast waves, the development of a realistic surrogate human head and brain, the data acquisition system which include the instruments needed to correctly identify and measure the attenuation of the pressure/blast waves in the head/brain and the analysis of the data acquired.

In designing the experiments, the RED Head (Realistic Explosive Dummy Headform) was fixed with strain gauges on the exterior to check for stress waves in the surrogate skull, and with a fiber optic sensor inside the brain for pressure measurement. Making use of a shock tube facility, there were 11 shots fired at different breech pressures, the lowest using a 0.01-inch Mylar® burst membrane and the highest using ten 0.01-inch Mylar® burst membranes. The results were then tabulated and presented; the aim is to study the propagation of blast waves and their attenuation within the experimental headform with a simulated brain.

This thesis is dedicated to my mother Victoria Sogbesan,
for her relentless sacrifices and continuous support.

Acknowledgement

The author wishes to thankfully acknowledge the contributions of:

The Almighty God for the strength to complete this thesis.

Dr. Carl A. Nelson for his sincere supports, guidance and advice, and his continuous help in all matters concerning this research.

Dr. Jeffrey Shield and Dr. John Barton for their advice and general support regarding the entire research and for their moral and academic supports.

Members of my examining committee, Dr. Linxia Gu and Dr. Wieslaw Szydlowski for their assistance and for reviewing this research work and their inputs, comments and guidance.

Dr. Mehrdad Negahban, Dr. Ruqiang Feng, Dr. Joseph Turner, Dr. Mickael Arnoult and Dr. Namas Chandra, for their inputs and comments during the entire research.

Mamur Hossain; for his help in setting up for the experiments, Matt Nienaber; for helping out with experiments and instrumentation troubleshooting, Aaron Alai, Aaron Holmberg, and Nick Kleinschmit; for their help with the shock tube, and Jonathan Hein; for his assistance with the MTS and ARAMIS® machines. And other members of the UNL Trauma Mechanics Research Laboratory; for their assistance on this project.

The Dept. of Mechanical Engineering Faculty, Staff and other personnel, for logistics with instrumentation orders and supports, especially Ms. Nan Rowe and Ms. Janet Renoe.

The UNL office of Graduate Studies, for the reviews of this research work. The Army Research Office for sponsoring this research and my Master's degree.

And to family members, friends and other colleagues for their moral support throughout my entire Master's degree, comments, remarks, and their encouragement during the difficult times of putting this research work together.

Thank you and may God bless you all.

Table of Contents

Abstract.....	ii
Acknowledgement.....	v
Table of Contents.....	vii
List of Figures	x
List of Tables	xiv
Chapter 1: Introduction	
1.1: INTRODUCTION.....	16
1.2: MOTIVATION	17
1.3: OBJECTIVE	18
1.4: THESIS ORGANIZATION.....	19
Chapter 2: Literature Review	
2.1: TBI	20
2.2: IEDs.....	21
2.3: SHOCKWAVE	23

2.4: BLAST INJURY	23
2.5: HEAD PROTECTION.....	27
2.6: OTHER RESEARCH WORK	29
Chapter 3: RED Head Development	
3.1: THE HUMAN BRAIN	36
3.2: RED HEAD.....	38
3.3: MATERIAL MODELING.....	40
Chapter 4: Instrumentation	
4.1: INSTRUMENT SELECTION	43
4.2: PVDF SENSORS.....	44
4.3: STRAIN GAUGES	45
4.4: MICRO ELECTRO-MECHANICAL SYSTEMS (MEMS) ACCELEROMETERS	49
4.5: FIBER OPTIC SENSOR	51
4.5.1: FABRY-PÉROT FIBER OPTIC GAUGES.....	53
4.6: DATA ACQUISITION SYSTEM.....	55

4.6.1: HARDWARE.....	56
4.6.2: PRINCIPLE OF THE VELOCE SIGNAL CONDITIONER.....	58
4.6.3: RELATIVE CONDITIONER VERSUS ABSOLUTE CONDITIONER.....	60
4.7: CALIBRATION.....	62
Chapter 5: Results and Analysis	
5.1: INITIAL TEST.....	71
5.2: TEST/EXPERIMENT DESIGN	72
5.3: METHODS	74
5.4: RESULTS, PLOTS AND TABLES	79
5.5: DISCUSSIONS	85
Chapter 6: Conclusions	
6.1: CONCLUSIONS.....	91
6.2: FUTURE WORK.....	93
Works Cited.....	95
Appendix.....	102

List of Figures

Figure 2.1: Causes of TBI.....	20
Figure 2.2: An image of 500lbs bomb rigged as an IED.....	22
Figure 2.3: A blast explosion.....	26
Figure 2.4: Advanced combat helmet.....	29
Figure 2.5: Livermore Lab simulations of a blast-induced TBI.....	30
Figure 2.6: Pressure contours showing the effect of a front-facing blast at various times after detonating 1.5kg of C4 from a distance of 3m.....	31
Figure 2.7: Simulations show that the older suspension-type helmet amplifies the blast pressure under the helmet.....	33
Figure 2.8: In simulation of a blast such as an IED an unprotected skull ripples where the pressure inside the skull is highest.....	34
Figure 3.1: The major areas of the brain have one or more specific functions.....	36
Figure 3.2: 3D CAD Design of RED Head.....	39
Figure 3.3: RED Head skull assembly (a) Inside view (b) Isotropic view.....	39

Figure 3.4: The Realistic Dummy (RED) Head (a) left view (b) right view (c) back view.....	42
Figure 4.1: The schematic for the experiment set up, showing the data acquisition system.....	43
Figure 4.2: A Piezotech® PVDF piezoelectric sensor.....	44
Figure 4.3: A 350-ohm strain gauge quarter bridge wiring.....	45
Figure 4.3.1: Strain gauge attachments on the skull flexure of the RED Head.....	46
Figure 4.3.2: CAD Design of the Junction box.....	48
Figure 4.3.3: Junction box for the strain gauge.....	48
Figure 4.4: MEMS Accelerometer.....	49
Figure 4.5: FISO® fiber optic sensor	52
Figure 4.5.1: Non-compensated pressure gauge.....	53
Figure 4.6: A screen capture of the Matlab® software used in data processing.....	55
Figure 4.6.1: Standard 8-Slot PXI Chassis containing an embedded system controller and seven peripheral modules.....	57
Figure 4.6.2: Schematic of the operation of the Veloce® conditioner.....	59

Figure 4.6.3: Schematic explanation of relative measurement conditioners.....	61
Figure 4.7: The MTS machine.....	63
Figure 4.7.1: Kolsky bar test set up.....	63
Figure 4.7.2: Kolsky bar test with the pressure sensor embedded in the Jell-O material.....	63
Figure 4.7.3: Kolsky bar test plot.....	65
Figure 4.7.4: Polycarbonate cylinder test plot.....	68
Figure 4.7.5: CAD Design of the polycarbonate cylinder.....	69
Figure 4.7.6: The set up for calibrating the BCMs	70
Figure 5.1: RED Head blast test with Skin and No Skin results comparison.....	71
Figure 5.2: Placement of the FISO® Sensor	73
Figure 5.2.1: Arrangement of the Strain Gauges on the RED Head	74
Figure 5.3: Red Head set up.....	75
Figure 5.3.1: Part of the data acquisition system set up for the strain gauges, this include the junction box, signal amplifiers, power supply and a DAQ.....	76
Figure 5.3.2: Set up of the Data acquisition system, with (a) PXI, (b) Signal conditioners, and (c) Display unit.....	77

Figure 5.3.3: Shock wave generator.....	78
Figure 5.3.4: The ideal shocktube, showing types of waves present when the membrane ruptures.....	78
Figure 5.4.1: Blast test #1 (lowest) with pressure measurement.....	80
Figure 5.4.2: FISO® sensors 1 and 2 measurements from blast test #1.....	80
Figure 5.4.3: FISO® sensors 3 and 4 measurements from blast test #1.....	81
Figure 5.4.4: Blast test #1 (lowest) with lateral hoop strain readings.....	81
Figure 5.4.5: Blast test #1 (lowest) with vertical strain measurement.....	82
Figure 5.4.6: Blast test #10 (highest) with pressure measurement.....	82
Figure 5.4.7: FISO® sensors 1 and 2 measurements from blast test # 10.....	83
Figure 5.4.8: FISO® sensors 3 and 4 measurements from blast test #10.....	83
Figure 5.4.9: Blast test #10 (highest) with lateral hoop strain readings.....	84
Figure 5.4.10: Blast test #10 (highest) with vertical strain measurements.....	84
Figure 5.5: Quarter-Bridge Circuit.....	85

List of Tables

Table 2.4.1: Etiology of Blast Injury.....	24
Table 2.4.2: Type of Traumatic Brian Injury.....	25
Table 3.1.1: Mechanical properties of various parts of the human head.....	37
Table 3.2.1: Dimensions of the RED Head.....	38
Table 3.3.1: Material properties for the human skull and brain.....	40
Table 3.3.2: Material properties for the human brain.....	41
Table 4.1.1: Strain gauge dimensions.....	47
Table 4.5.1: Fiber optic gauge vs. PVDF gauge.....	54
Table 4.7.1: Calibration report of FISO® 1010032209 fiber optic sensor with gauge factor 6011732 and sensitivity of 17.32nm/psi	64
Table 4.7.2: Calibration report of FISO® 1010032208 fiber optic sensor with gauge factor 6011710 and sensitivity of 17.10nm/psi	64
Table 4.7.3: Error table from the Kolsky bar test.....	66

Table 4.7.4: Mechanical properties comparison for cylinder test design.....67

Table 5.3.1: Shock Tube configuration results.....79

Chapter 1: Introduction

1.1: INTRODUCTION

High pressure blast waves can cause significant damage to organs of military personnel exposed to improvised explosive devices (IED) [1, 2]. Not until recent times have the brain been the focus of research related to blast wave injuries, because mortality rates were on the increase and brain injury was somewhat secondary. Today, the precise mechanisms for brain injury from blast/pressure waves still remain a mystery. One thing that is certain is that improved helmets and body armor protect our soldiers from shrapnel, bullets and fragments but not blast waves, so what otherwise could have been a result of many deaths are now reduced to brain injury cases only [3]. About 65% of war veterans wounded in action in both Afghanistan and Iraq are affected by injuries from improvised explosive devices and between 10 and 20% of Iraq war veterans have suffered from some sort of head trauma from blast/pressure waves [2].

Sponsored by the Army Research office, scientists around the world are busy trying to find the associations between pressure waves and traumatic brain injury (TBI). Researchers and scientists at Livermore National Laboratory used simulations to study the effects of blast on the deformation of the skull and are using the same technology to investigate the mechanisms of TBI as a result of blast waves [3].

Direct recording of pressure waves inside the brain during exposure has not been recorded previously, but Chavko et al. measured pressure waves inside the brain of a rat using fiber optic sensors, one of the sensors this research used[2].

To gain a better understanding of the mechanisms responsible for blast-induced TBI and to design and develop a more effective head protection system, we would require more detailed data describing typical blast events and their effects on soldiers. Sensors currently in use by the military to measure blast waves are large, heavy and sometime unreliable because of their placement around the helmet [4]. Human cadavers or animal test subjects have proven unreliable [6]. So there is no real blast data within the brain available from the war zone to correlate with TBI data. One of the questions built into the experiment design is to distinguish the differences between blast wave trauma and impact trauma. The thesis will be taking a look at some of the experiments designed to simulate a blast wave comparative to the one given off from an IED, with special emphasis on interaction with a head model.

1.2: MOTIVATION

There have been limitations in getting an accurate measurement on an injured soldier that has just been exposed to a blast wave; however, researchers for years have used cadavers and animals instrumented for experimentation. Cadavers have limited duration of viability, they cannot typically be used multiple times, and there are differences from body to body; hence it is extremely difficult to achieve reliable comparison of data. Animal testing such as in rats [2] has proven useful, but testing in humans, pigs and other mammals have proven difficult [6].

Understanding the impacts of blast wave in the brain could lead to understanding the best form of protection the head needs in such a scenario. Developing an accurate mathematical model suitable for the simulation of the mechanical behavior of the human brain under blast loading conditions could lead to significant advances. These new discoveries could revolutionize the way we look at soldier safety and future combat protection. It could also introduce new knowledge in fluid mechanics and biomaterials. It will broaden existing research into brain trauma conditions under blast loading, which will improve tremendously current treatment decisions for basic brain-related problems such as TBI and PTSD experienced by returning combat troops [6].

1.3: OBJECTIVE

Due to the unpredictable nature of pressure waves in the human head, it is imperative that a stable and accurate system be put in place to understand this phenomenon. All gas dynamic conditions vary through a blast wave, and most have role in target loading, so it is important to have some sort of reliable way to measure blast and its impact. Blast gauge measurements are vulnerable to wide ranging interference effects, most of which are inherently severe in blast environments, especially from temperature, shock/vibration, casing stress, etc. [7]. That is why the design and analysis of the data must be done in the most acceptable environment. The design of the experiments, data acquisition and instrument selection has to be optimal in the most extreme condition.

The main objective of this research is to evaluate the propagation effects of pressure/blast waves in the brain. The goal is to investigate the effects of pressure/blast waves, particularly those typical of IEDs, on the human brain and the effects of the waves

on potential causes of TBI. The intent is to analyze the results in predicting mild TBI as a function of incident blast.

A sub-objective is to design and select the best instrument and data acquisition system that is capable of taking accurate measurements under such conditions and to design the experiments that satisfy the main objective.

1.4: THESIS ORGANIZATION

The thesis is organized in such a way as to highlight our current and ongoing work on the project, and future work will also be discussed at the end of the report. The results from different experiments and calibration tests will be included.

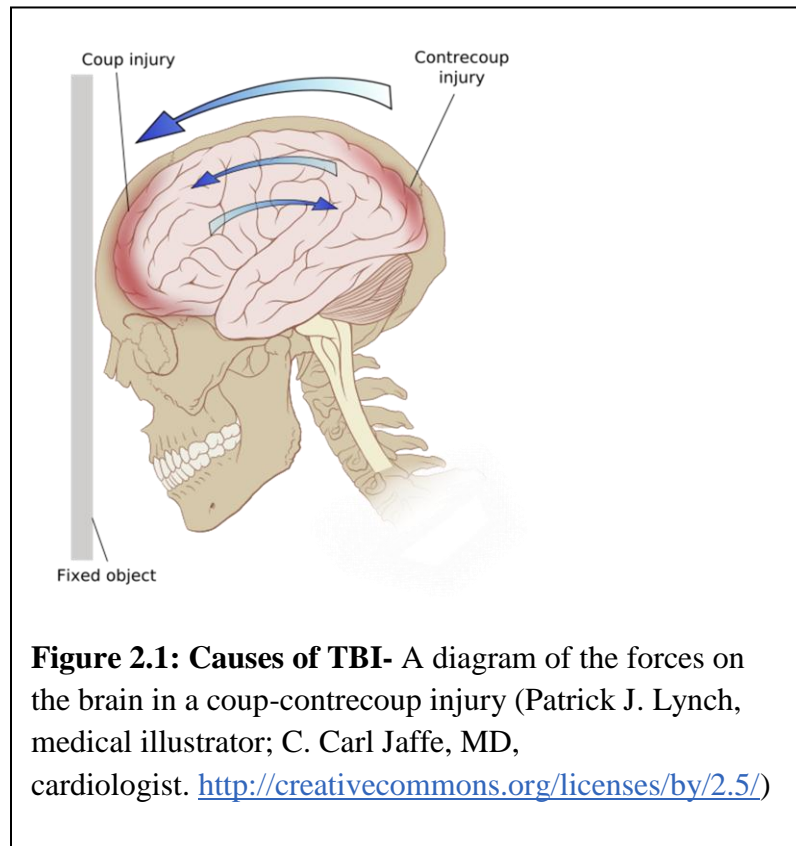
The first part of the thesis takes a look at the various literature detailing the causes and effects of TBI, the dangers of improvised explosive devices, and description of shockwaves and how they propagate. The history of head protection and current scientific breakthroughs in soldier protection are also presented.

The second part takes a look at my contributions to surrogate brain material selection and design of the RED Head (realistic explosive dummy head) system. The selection of instruments and their calibration forms the later part of the research. The corresponding results, data and plots make up the third part of the research with conclusions and discussion on the project finalizing the thesis.

Chapter 2: Literature Review

2.1: TBI

Traumatic Brain Injury (TBI) can be the result of a direct blow or jolt to the head, and also by advancing pressure waves and direct impulses or impact. It is also called intracranial injury. TBI is a major health concern worldwide, especially in infant death and disability [8]. It can cause functional changes with consequences as varied as aggressive social behavior, impaired thinking, language, learning, emotions, behavior, sensation, and neuro-degenerative diseases such as epilepsy, Alzheimer's disease, Parkinson's disease, and other brain disorders that become more prevalent with age [9,



10]. Brain trauma causes secondary injury, in addition to the damage caused at the moment of injury, within minutes and days after the initial event. These alterations in cerebral blood flow and/or pressure buildup within the skull can which contribute substantially to the damage from the initial injury [11].

The major leading causes of TBI are falls, which account for about 28% of cases, motor vehicle-traffic crashes (20%) being struck by/against a heavy object (19%) and assaults (11%) [8].

According to the Brain Injury Association, every 23 seconds, one person in the US sustains TBI and an estimated 3.17 million Americans currently live with disabilities resulting from TBI. Out of the 1.4 million Americans who sustain head injuries each year, more than 50,000 people die as a result of Traumatic Brain Injury [8].

High-pressure waves (blast) as a result of improvised explosive devices from terror attacks account for the majority of combat injuries, both from Afghanistan and Iraq [12].

These pressure waves could produce human brain damage.

2.2: IEDs

IEDs can penetrate even highly protected structures, including sophisticated battle tanks and heavily armored vehicles. Some IEDs utilize very heavy artilleries and explosive devices, which are often buried below a dirt surface and are activated via remote control. IEDs usually combine the effects of blast, fragmentation and armor

penetration, through the use of shaped charge liners. Camouflaged explosives can also serve as roadside bombs. These devices are remote controlled, triggered by infra-red, pressure bars or trip wires and are aimed to delay or disrupt enemy forces in their movement into a secured area [12].

Blast injury as a result of terrorist attacks or military conflict has increasingly become a worldwide concern [13].



Figure 2.2: An image of 500lbs bomb rigged as Improvised Explosive Device (IED). Source: Globalsecurity.com
(http://www.globalsecurity.org/military/intro/images/ied-iraq_500lbs-bomb_2004120107a_hr.jpg)

2.3: SHOCKWAVE

This is an exothermic supersonic blast accelerating through a medium that eventually drives a pressure wave propagating directly in front of it. Blast is the process by which “*energy of an explosion source that is propagated into its surrounding environment then interacts, loads and damages materials, structures and systems*” Shockwaves develop as a result of pressure build up in compressible flow or as a way to balancing a forced pressure mismatch in the system [7].

When a shockwave is generated, there are nearly discontinuous changes in the total pressure, density, and particle speed across the shock front [14].

The shock wave we are working with is assumed to be planar and fully developed from the origin till it exits the tube, covering the entire 9” square shocktube.

2.4: BLAST INJURY

The damage potential of an explosive blast depends on three main factors: the force exerted on the target, the duration of the applied force and the ability of the target to withstand the effects of the blast wave [16].

Blast injury is divided into three main categories. Primary blast injury is as a result of the over-pressurization wave from the explosion. The injury is caused by pressure differentials at density interfaces such as air-fluid contact. The tympanic membrane is the most frequently injured structure in primary blast injury, followed by the

lungs, colon, and small bowel [1, 13]. For soldiers with body protection, few report injury caused to gas-containing organs such as lungs [7].

Secondary blast injury occurs when objects in the blast area become projectiles capable of inflicting both blunt and penetrating injury, while tertiary injury results from a powerful blast wind that seems to throw the patient away from the blast epicenter with sufficient force to cause traumatic impacts with nearby objects [13].

Bochicchio et al. [13] evaluated the epidemiology of blast injury in a domestic non-terroristic scenario. Their data were analyzed retrospectively on patients admitted with different types of blast injury over a 10-year period at a busy urban trauma center. Injuries were classified by etiology of explosion and anatomical location.

Etiology	Number of Patients
Private dwelling explosion	31 (35%)
Industrial pressure blast	20 (22%)
Industrial gas explosion	16 (18%)
Military training explosion	15 (17%)
Home explosive device	8 (9%)
Fireworks explosion	1 (1%)

Table 2.4.1: Etiology of Blast Injury [13]

Eighty-nine cases of blast injury were identified in 57,392 patients (0.2%) treated over the study period. The majority of patients were male (78%) with a mean age of 40 +/- 17 years. The mean Injury Severity Score was 13 +/- 11 with an admission Trauma and Injury Severity Score of 0.9 +/- 0.2 and Revised Trauma Score of 7.5 +/- 0.8. The mean intensive care unit and hospital length of stay was 2 +/- 7 days and 4.6 +/- 10 days, respectively, with an overall mortality rate of 4.5 per cent [13].

Types of Injury	Number
Cerebral contusion	13
Subdural hematoma	8
Diffuse axonal injury	4
Subarachnoid hemorrhage	3
Intracerebral hemorrhage	3
Epidural hematoma	3
Intraventricular hemorrhage	2

Table 2.4.2: Type of Traumatic Brain Injury [13]

Historically, TBI has been associated with secondary or tertiary blast injury; Bochicchio et al. [13] suggested that the central nervous system may be significantly affected by primary blast injury. The report highlighted that domestic blast injury occurs only on a smaller scale on a regular basis within the United States, and that non-terrorist sources of blast injury such as from explosions involving natural gas, industrial plant accidents, legal and illegal fireworks, mining and demolitions work, and homemade explosives for personal or criminal use are a small fish in the pond when compared to numbers from the war front [13].

Whether delayed or immediate, the effects of primary blast injury on air-filled organs include pulmonary contusion and hemorrhage as well as gastro-intestinal tract injury or perforation. It has also been observed to cause significant damage to sensorineural pathways as well as the inner ear [13].

A review of soldiers injured in conflict in Lebanon [13] reported that nearly one third of 17 blast-injured patients were diagnosed with diffuse brain injury. 52 percent of critically injured patients of the Madrid bombings of March 11, 2004 were diagnosed with head injuries, and 13.5 percent of surviving victims of the Oklahoma City bombing in 1995 also sustained some sort of head injury [13].

Prior studies have clearly demonstrated that even mild TBI may lead to cognitive



Figure 2.3: A blast explosion (Source: <http://www.newscientist.com/blog/invention/2007/07/blast-wave-protection.html>)

and emotional impairment requiring treatment, but study results suggested that TBI induced by blast injury is a dynamic process that continues to evolve well after the time of injury: *“Thirty per cent of 665 patients from Yugoslavia sustaining blast injury reported subjective neurological or psychological symptoms after injury, and war veterans exposed to blast injury in the remote past have been shown to demonstrate persistent electroencephalographic changes consistent with TBI.”* These findings suggest that blast may produce subtle brain injury, which is not immediately obvious on clinical presentation but may lead to cognitive deficits post injury [13].

2.5: HEAD PROTECTION

Protective helmets protect the wearer’s head by absorbing mechanical energy and protecting against penetration. Anatomical helmets adapted to the inner head structure were first invented by neurosurgeons at the end of the 20th century. The first military use of helmet was around 950 A.D. Today, military helmets are made of ballistic materials such as Kevlar, which have excellent bullet and fragment stopping capabilities and also offer non-ballistic protection against other forms of trauma and shock waves.

“The M1 helmet is a combat helmet used by the American military from World War II until it was replaced by the PASGT helmet beginning in 1985”[17].

Personnel Armor System for Ground Troops (PASGT) was developed in 1975 and it’s a combat helmet and ballistic vest used from around 1983 until 2003 by the American military. *“The shell is made from 29 layers of Kevlar consisting of a*

ballistic aramid fabric treated with a phenolic resin system and it offers protection against shrapnel and ballistic threats". It meets the Department of Defense test method standards for armor and helmet (MIL-STD-662 F). It weighs between 3.1 pounds and 4.2 pounds [17].

"The lightweight helmet" is the replacement for the PASGT combat helmet. It is identical in shape to the PASGT and heavier than the advanced combat helmet (ACH), a Kevlar® type protective helmet and its larger size also offers more protection, it is also lighter than the PASGT. The Marines started using it around 2004 and it completely replaced the PASGT in 2009 [17].

"The Modular Integrated Communications Helmet (MICH), commonly known as the Advanced Combat Helmet (ACH), was developed by the United States Army Soldier Systems Center to be the next generation of protective combat helmets for use by the United States Army. The difference between MICH and ACH are the communications components which ACH lacks" [17]. The current form of military helmet system has provided the desired protection to US troops. However, there is still a critical need to drastically mitigate traumatic brain injury among surviving soldiers wounded during combat operations, especially in Iraq and Afghanistan [18].

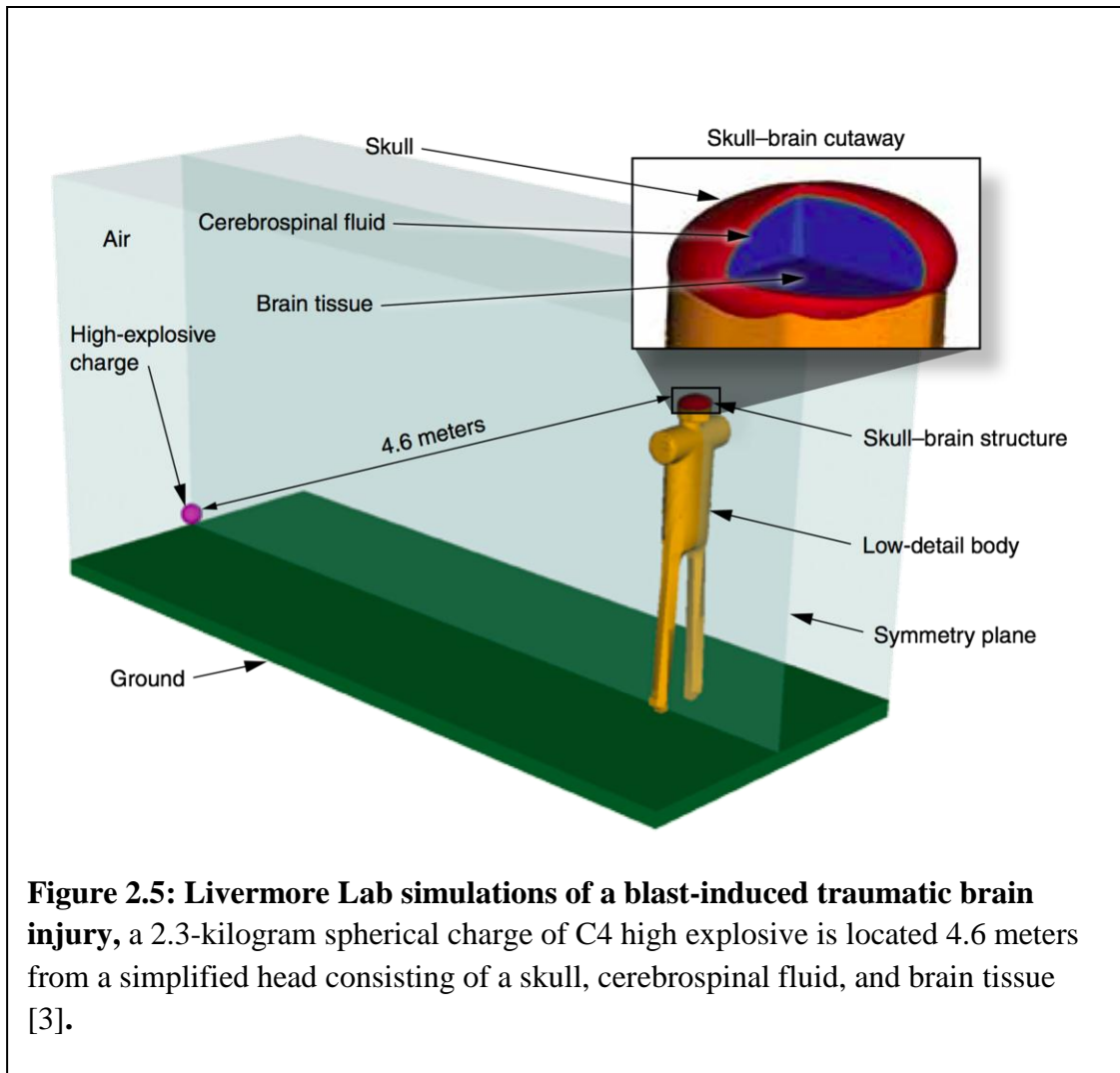


Figure 2.4: Advanced Combat Helmet (Source: www.fy-composites.com)

2.6: OTHER RESEARCH WORK

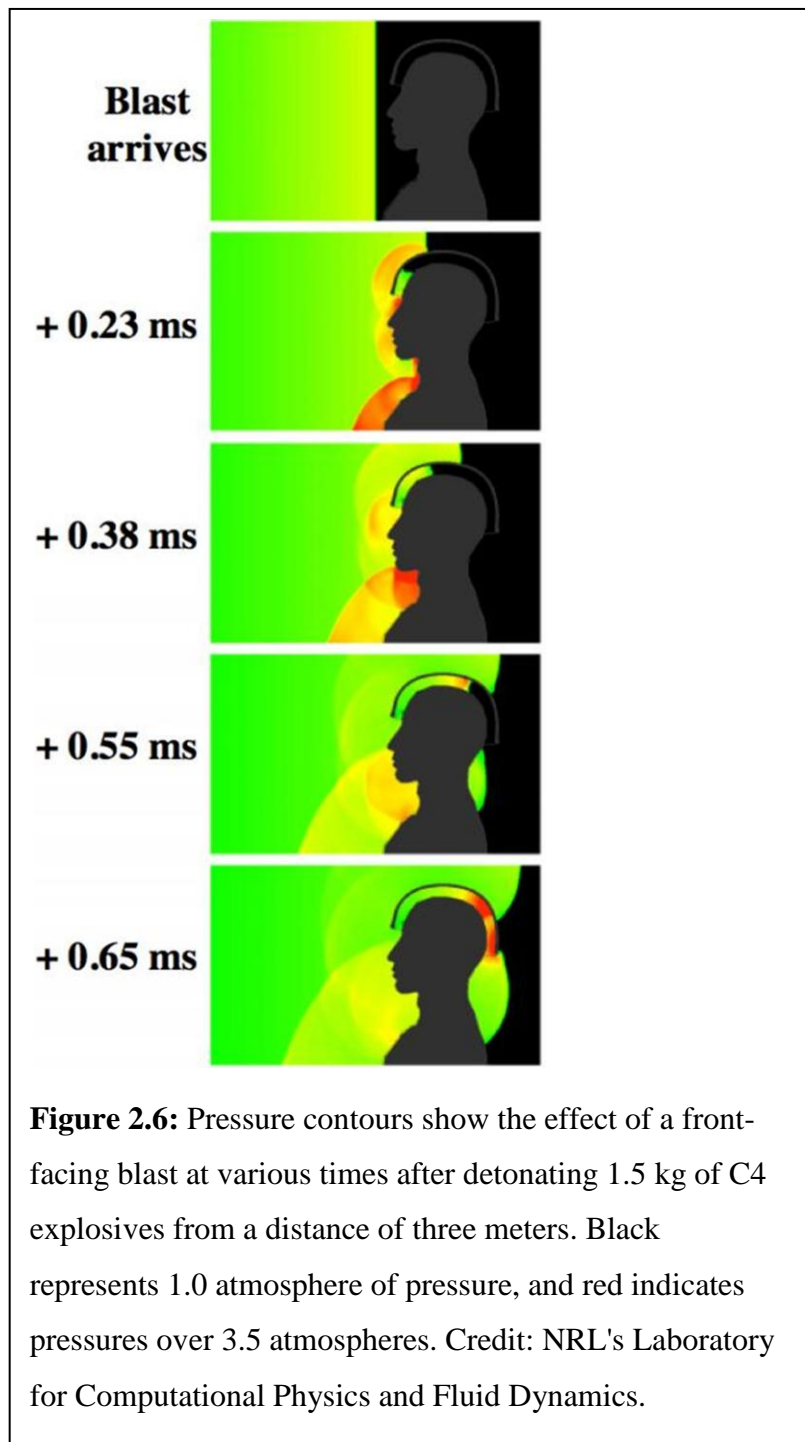
Coordinated experiments and numerical simulations investigated the pressure field surrounding a head with a helmet subjected to a blast wave typical of injurious but non-lethal threats. Mott et al. [19] conducted experiments with C4 explosive charges ranging from 0.75 kg to 5 kg, and two anthropomorphic test mannequins (Hybrid III) located 3 m from the explosive. Pressure sensors were mounted at selected locations around each the free-field and the mannequin's head. The blast and ground reflection were numerically modeled and the results used as a boundary condition for a three-dimensional unsteady simulation of the head-helmet complex subjected to a blast wave. The helmet showed good protection against primary blast injury both in simulations and experiments. However, the pressure waves entering the gap between the helmet and the

head were congregating on the side and the back of the head and the measurement at those points acted as if they were unprotected surfaces subjected to blast waves [19].



In a similar experiment, Livermore National Laboratory with the aid of sophisticated computerized hydrodynamic codes is helping researchers understand the mechanisms of TBI [3]. They simulated a military helmet under blast conditions, and noted how the shockwave was able to wash under the helmet through the gap created by the web suspension which is essential for ballistic protection. This under wash effect

focuses the blast wave, causing pressure under the helmet to exceed that on the outside [3]. This is due to a combination of the increased projected helmet area blocking the shock and having foam padding between the helmet and the head, something that does not exist at the ear location [19].



Other TBI simulation at Livermore unexpectedly revealed that the skull flexes when exposed to a nonlethal blast wave, even one generating pressures as low as 1 atmosphere (or 100 kilopascals) above ambient pressure. In fact, even without direct head impact, nonlethal blasts induce enough skull flexure to generate some potential brain damage [3].

The numerical simulation used to describe and explain the pressure and flow-field around the head and helmet of a soldier exposed to a blast wave is the compressible Euler equations with species transport [19]:

$$\frac{\partial \rho}{\partial t} + \nabla \cdot \rho \mathbf{v} = 0 \quad (\text{Equation 1})$$

$$\frac{\partial \rho \mathbf{v}}{\partial t} + \nabla \cdot \rho \mathbf{v} \mathbf{v} = -\nabla P \quad (\text{Equation 2})$$

$$\frac{\partial E}{\partial t} + \nabla \cdot (E + P) \mathbf{v} = 0 \quad (\text{Equation 3})$$

$$\frac{\partial n_k}{\partial t} + \nabla \cdot n_k \mathbf{v} = S_k \quad (\text{Equation 4})$$

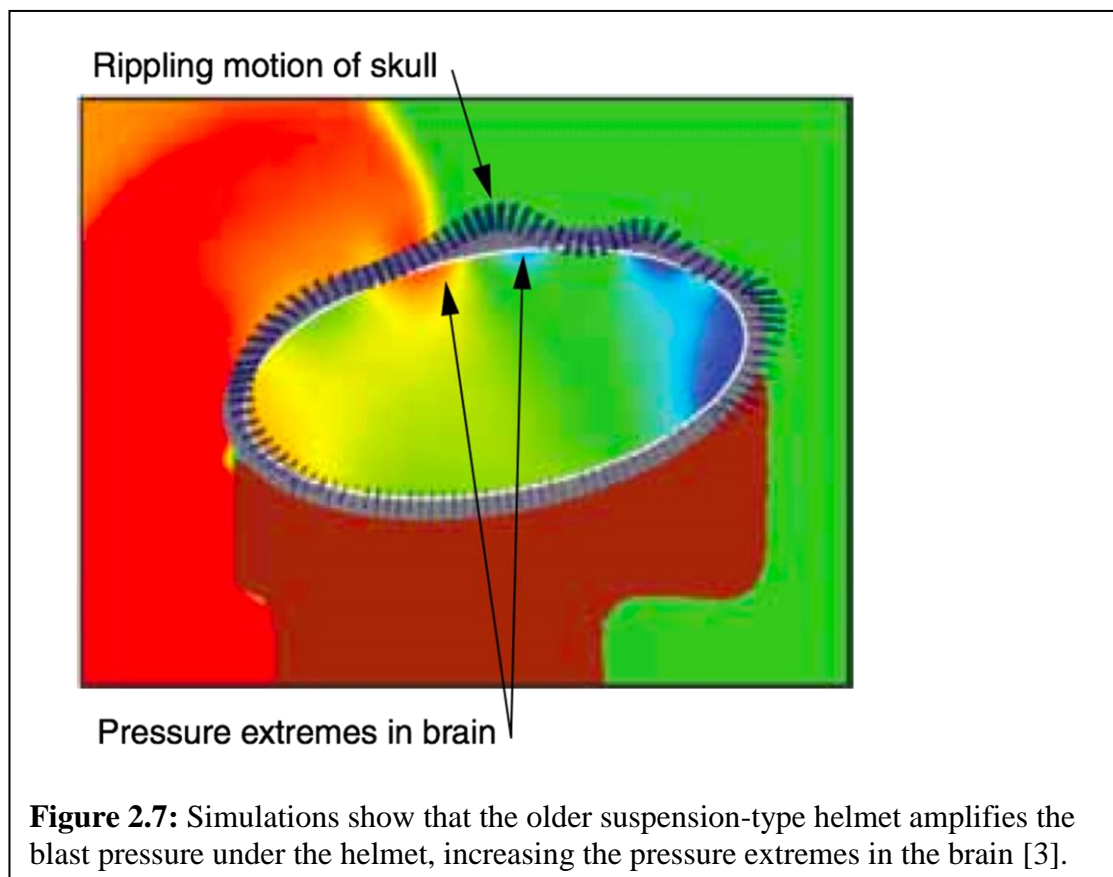
where ρ is the total density of the mixture, \mathbf{v} is the bulk velocity, E is the total energy, P is the thermodynamic pressure, n_k is the concentration of species k , and S_k is the chemical source for species k .

Total enthalpy is:

$$E = \sum_{k=1}^N n_k h_k(T) - P + \frac{1}{2} \rho \mathbf{v} \cdot \mathbf{v}$$

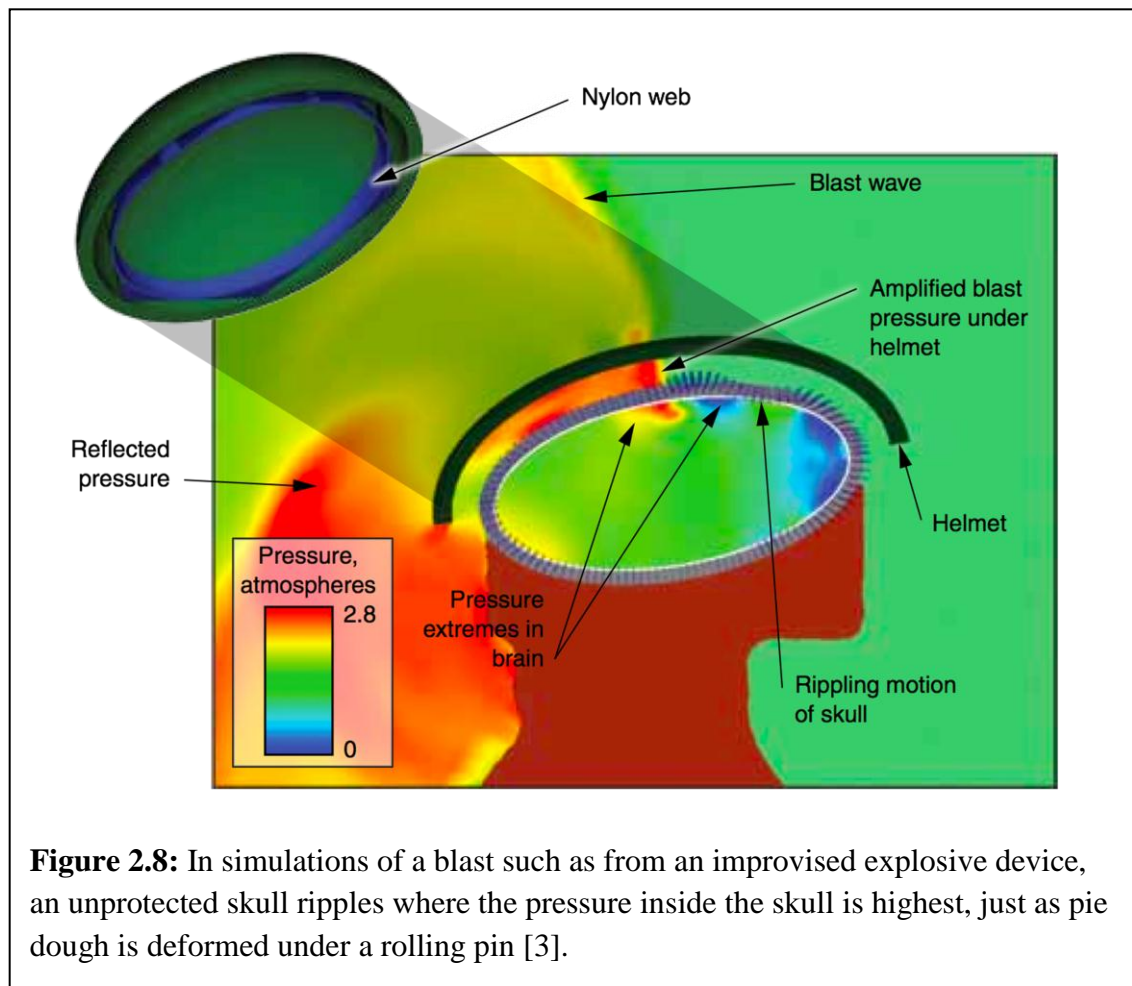
(Equation 5)

where the species enthalpy, $h_k(T)$ are computed from 6th-order polynomial curve fits.



The Mach number of a shockwave is the ratio of its inertia to compressibility. It is the non-dimensional factor governing resistance due to longitudinal (compression) wave formation that is the ratio of the speed of flow (v) to the speed of sound in a fluid (c).

$$M = v/c \quad \text{(Equation 6)}$$



Shock waves are generally formed in the shock tube when a fluid is heated so rapidly that the leading edge of its expansion travels at or above the speed of sound in the fluid. “*Roughly spherical shock waves form when bombs, fireworks, and other*

pyrotechnic devices explode. A bolt of lightning generates a cylindrical shockwave centered on the bolt's path” [22].

The formula to compute Mach number in a supersonic compressible flow is derived from the Rayleigh supersonic Pitot equation:

$$M = 0.88128485 \sqrt{\left(\left(\frac{q_c}{P}\right) + 1\right) \left(1 - \frac{1}{7M^2}\right)^{2.5}} \quad (\text{Equation 7})$$

where:

M is Mach number

q_c is impact pressure measured behind a normal shock and

P is static pressure.

Impact pressure is the difference between Pitot pressure (also known as stagnation pressure or total pressure) and static pressure. Generally, M for shockwaves is greater than 1 but not more than 5.

The general wave speed calculation for a solid could be employed for our experiment as:

$$c = \sqrt{\frac{K}{\rho}} \quad (\text{Equation 8})$$

where K = bulk or shear modulus

ρ = density

Chapter 3: RED Head Development

3.1: THE HUMAN BRAIN

The most important part of the human head is the brain. It is the center of the nervous system and an extraordinary and complex organ. Its full characteristics are still not well understood, despite increased knowledge and breakthroughs in the neurosciences [20]. The brain controls the other organ systems of the body, either by activating muscles or by causing secretion of chemicals such as hormones, but it is also an electrochemical and mechanical device [20]. It receives nervous signals from the senses, and responds

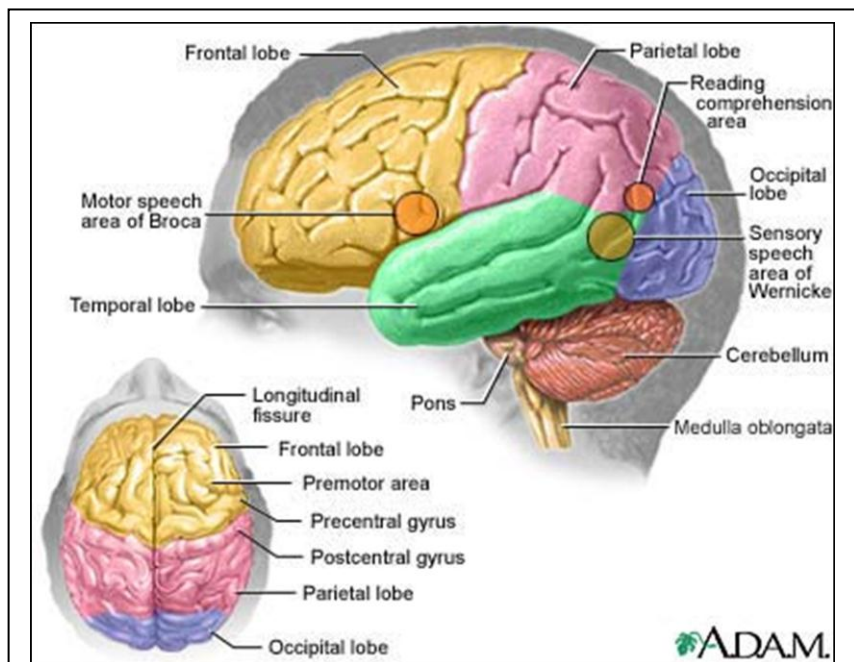


Figure 3.1: The major areas of the brain have one or more specific functions (A.D.A.M. Medical Illustration Team: Meredith Nienkamp, M.S.M.I., Dan Johnson, M.S.M.I., Lisa Higginbotham, M.S.M.I)

with signals that cause physical activity. The brain creates heat and chemical waste that are removed by a subsystem of drainage vessels [20].

The cerebrospinal fluid acts as a damping system. Layers of hair and skin over the skull also act as insulation from the effects of the sun and weather. The neck muscles complement the damping system, protecting against shocks and accelerations [20].

Units	Mass Density (kg/cm^3)	Modulus of Elasticity (Pa)	Poisson's Ratio	Shear Modulus (Pa)
Brain	1.05	2295	0.4	981
Cerebrospinal Fluid	1.00	2207	0.4	20
Blood	1.02	2236	0.4	20
Bone	1.33	9415×10^6	0.2	3432×10^6
Skin	1.03	1961	0.4	1961

Table 3.1.1: Mechanical properties of various parts of the human head [20]

The human head is composed of biological materials, each with their own mechanical properties such as elastic modulus, density, shear modulus, Poisson's ratio and magnetic permeability. Inside the head there is a delicate mechanical equilibrium involving pressure. This equilibrium can be disturbed by electromagnetic or mechanical waves. High frequency electromagnetic waves can cause perturbations in brain function. Tissues can also be affected by the accelerations and decelerations that make up mechanical waves [20].

3.2: RED HEAD

The Realistic Explosive Dummy (RED) Head is a surrogate human head form with simulated skull, skin and brain. It utilizes standard neck components from both the Hybrid 2 and Hybrid 3 Anthropomorphic Test Dummies (ATD) [21].

ATDs have been used for many years by the military, aerospace and automotive industries to assess and standardize safer protection systems [22]. In particular, the automotive industry over the years began research into creating the HYBRID system that seeks to replicate the physical properties of an adult human. The HYBRID system is an ATD developed by General Motors in 1971, when they decided to standardize the existing crash test dummies at the time “VIP-50” and “Sierra Stan” by combining their best features (hence the name hybrid) to model an average male in height, mass, and proportion.

Description	Dimensions
Neck	3.4 lbs
Head	10 lbs
Head Circumference	22.5 inches
Head Width	6.1 inches
Head Length	7.7 inches
Head Height	7.7 inches

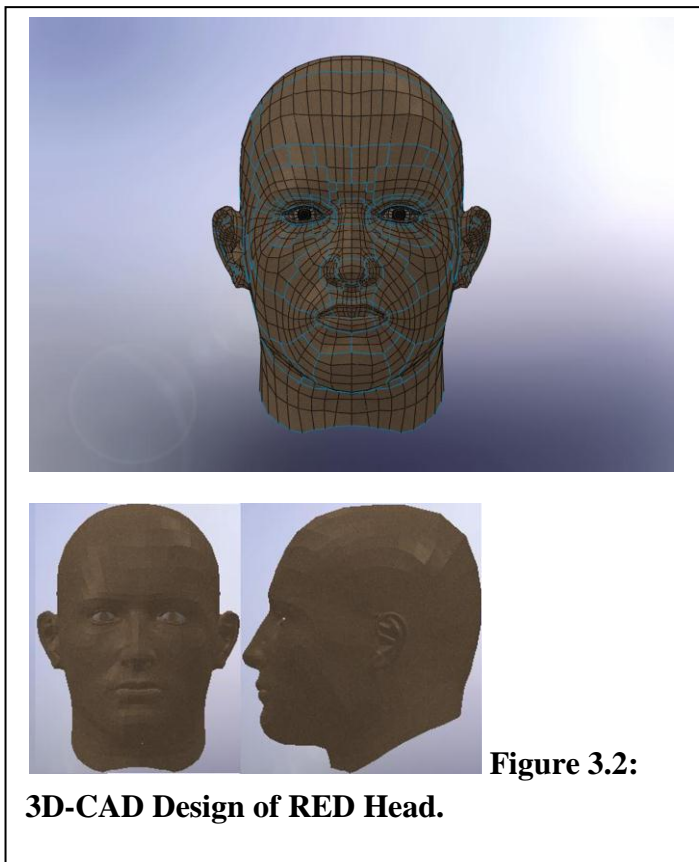
Table 3.2.1: Dimensions of the RED Head

Other ATDs developed for crash testing include: Side Impact Dummy (SID), Biofidelic Side Impact Dummy (BIOSID), and European Side Impact Dummy (EUROSID 1), and

US Air Force's Advanced Dynamic Anthropomorphic Manikin (ADAM) [22]. Manikin for Assessing Blast Incapacitation and Lethality (MABIL) was an ATD that was used to assess blast threats, especially in air-containing organs [23, 24].

The RED Head consists of a skull assembly with an opening for the brain and cerebrospinal fluid, and is attached to a base plate which is part of the neck assembly.

Table 3.2.1 represents the standard dimensions and weight of the RED Head. The head length and height are 7.7 inches while the width is 6.1 inches.



The neck and head assembly weighs about 13 pounds combined, while the head circumference is 22.5 inches. The head consists of a polyurethane skull and a polydimethylsiloxane (PDMS) skin. The head has a stainless steel base plate which contains a silicone rubber gasket. It is attached to a flexible neck structure that can simulate the movement of the neck in response to loading.

3.3: MATERIAL MODELING

The most important materials to model were the brain and the cerebrospinal fluid (CSF). Though it is important to represent all the different types of tissues found in the head, it is not a feasible feat to replicate all of them separately, even though they might have a non-negligible effect on blast wave transmission through the head [25]. The aim is to be as close as possible to the mechanical properties of the brain so as to provide an averaged brain response to blast loading. There are variations in parameter values when it comes to the mechanical properties of the human brain, depending on which author one is considering: there are some differences in the values provided (compare Tables 3.1.1 and 3.3.1) but the effect of this uncertainty on the work presented in this thesis is acceptable.

	Density (g/cc)	Initial Bulk Modulus (GPa)	Poisson's Ratio	Yield Stress (MPa)	Strain to Failure (%)	Fracture Stress (MPa)
Skull	1.412	4.82	0.22	95	0.8	77.5
Brain	1.04	2.37	0.49	--	--	--

Table 3.3.1: Material properties for the human skull and brain [29]

In doing this, we have to take a look at the properties of the brain tissue, the cerebrospinal fluid (CSF) and the skull in general. Many potential surrogate material properties were tested, and a few were found to be close to the brain, but some of these materials were not very stable in their properties over time [26]. Many researchers have modeled the CSF as an incompressible fluid and the brain parenchyma as a sponge of visco-elastic material [27]. Water was used to model the CSF because of its composition [28].

	Short-term Shear Modulus G_0 (kPa)	Long-term Shear Modulus G_∞ (kPa)	Decay Constant β (sec⁻¹)
White Matter	41.0	7.8	700
Gray Matter	34.0	6.4	700

Table 3.3.2: Material properties for the human brain [29]

Several materials including gelatin, toothpaste, custard powder and silicone gels were made and analyzed [26]. Step response analysis, rheometric analysis, and dynamic mechanical analysis (DMA) tests were performed to match up with existing data available for brain matter. The gelatins and silicone gels were closer in properties than any other material to the brain matter, and the silicone gels were much more stable than the water-based gels (gelatin).

A thinner-type additive gel was mixed with the silicone gels in order to match the dynamic modulus values to those of human brain matter [26]. This material developed in-house, forms the basis for our brain surrogate for testing.

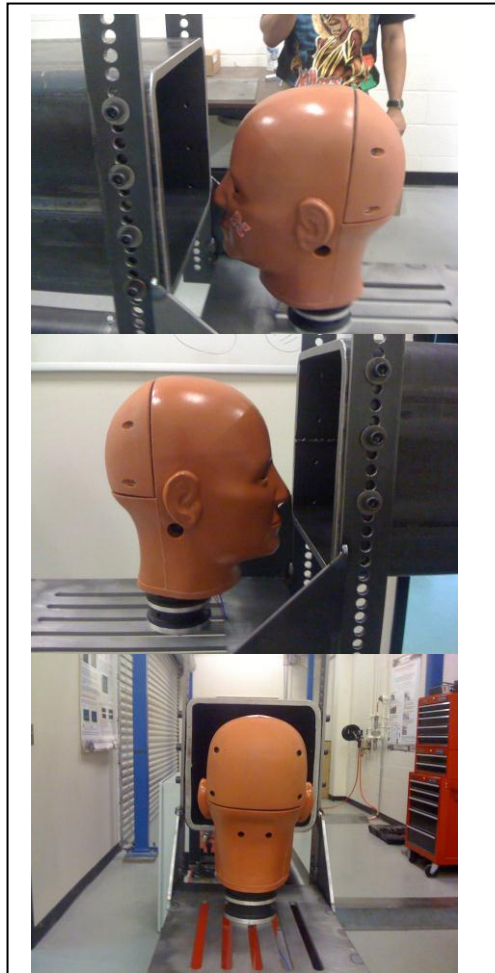
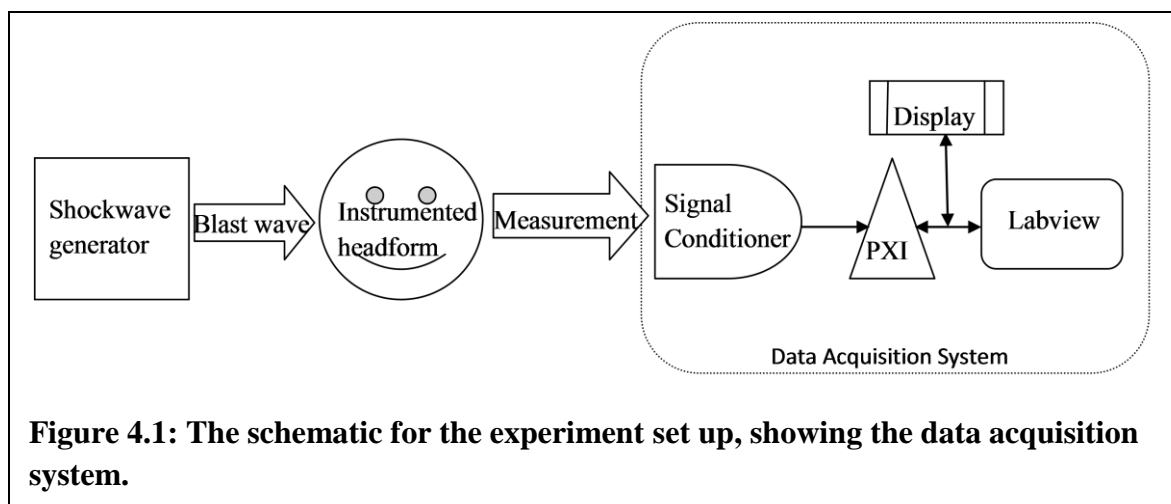


Figure 3.4: The Realistic Explosive Dummy (RED) Head, with left, right and back views.

Chapter 4: Instrumentation

4.1: INSTRUMENT SELECTION

As stated in chapters 2 and 3, trying to design an instrument or a data acquisition system needed to measure blast wave mechanisms in the head requires special handling and sensors small and sensitive enough to interpret the pressure waves received without distortion or any interference on the part of the sensor's geometry to the wave pattern. This system and design process relies on some instrument knowledge but also necessitates further investigation on current technology through review of existing literature. The experiment in itself is constrained, because of the environment in which it has to be performed with no flexibility in compromising the size of the sensors to use or the parameters that need to be measured. This process requires an understanding of available instruments, knowledge of the requirements of the signal to be measured, knowledge of the capability of the instruments, and a means for making an instrument



selection [30]. With all this in mind, optimal sensors and data acquisition system were selected suitable to process the shockwave reading and measurement.

4.2: PVDF SENSORS

Size was the first constraint concerning the sensors. They should be inserted into the brain surrogate and also positioned on the outside of the skull assembly of the RED Head in order to measure intracranial pressure and surface strain. The ideal sensor should be small in size and have negligible effect on what is being measured. The first sensor considered was a piezoelectric sensor referred to in this report as a PVDF sensor.

In 1969, Kawai [31] discovered strong piezoelectricity in polyvinyl fluoride (PVF) and polyvinylidene fluoride (PVDF) polymers, which become strongly ferroelectric after having been subjected to the effects of both mechanical stretching and the application of an electrical field [31, 32]. The polarization in the material generates the electric field, which then be used to transform the mechanical energy into electrical energy.

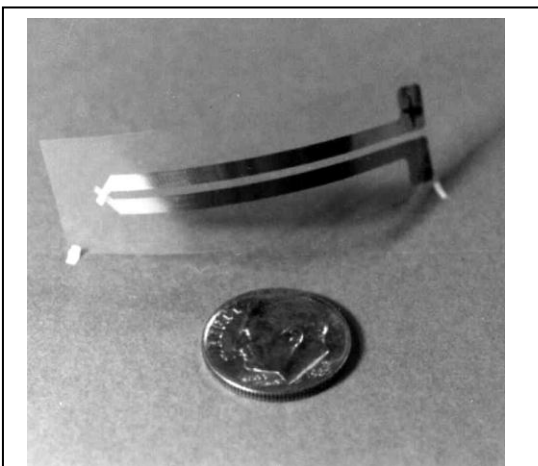
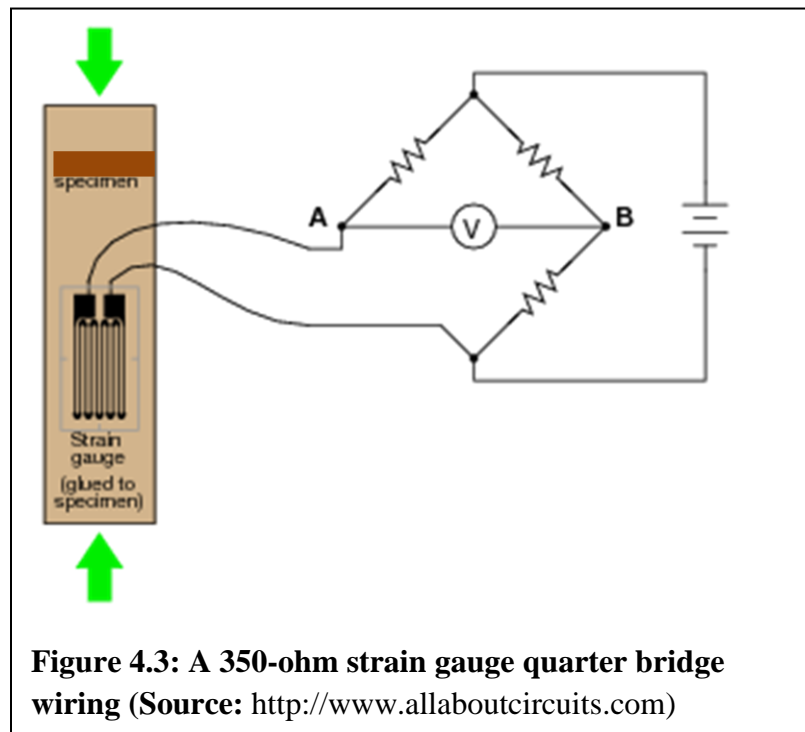


Figure 4.2: A Piezotech® PVDF piezoelectric sensor (Source: Piezotech S.A.S)

This sensor has been used in the past for shockwave measurements where it was exposed to very quickly rising high pressures up to 25GPa with a rise time of a few nanoseconds [33]. Although relatively thin, piezoelectric sensors were not ideal for insertion in the brain surrogate, firstly, because of their size and secondly because of their high noise ratio and the hysteresis in the signal [34].

4.3: STRAIN GAUGES

The second sensor considered was a strain gauge, to measure the strain induced by possible skull flexure. A strain gauge measures the change in electrical resistance of an object that has been subjected to applied stress. A change in resistance occurs when applied stress on the gauge in the direction of the orientation of the ‘zigzag-like’ conductive strip results in much higher strain over the effective length of the conductor



[35]. This resistance change is measured using a Wheatstone bridge. A Wheatstone bridge consists of 4 resistors in two circuit branches and is easy to build.

For our experiment we purchased a readymade bridge completion module (BCM) from Vishay® (**MR1-350-130**) so as to save time and avoid unnecessary lead wire errors and noise pick up, that are some of the common errors associated with handmade circuit production. The BCM was arranged with a 350-ohm quarter-bridge strain gauge input, having an excitation of up to 25 V but with a recommended range of 0.5 to 18 V, with an excitation voltage setting of 5 V. The Wheatstone bridge used in most strain gauge measurement circuits usually consists of the gauges for actively measuring the strains and the precision resistors incorporated in the measuring instrument for completing the circuit. A more symmetrical, balanced lead-wire system between the strain gauge circuit

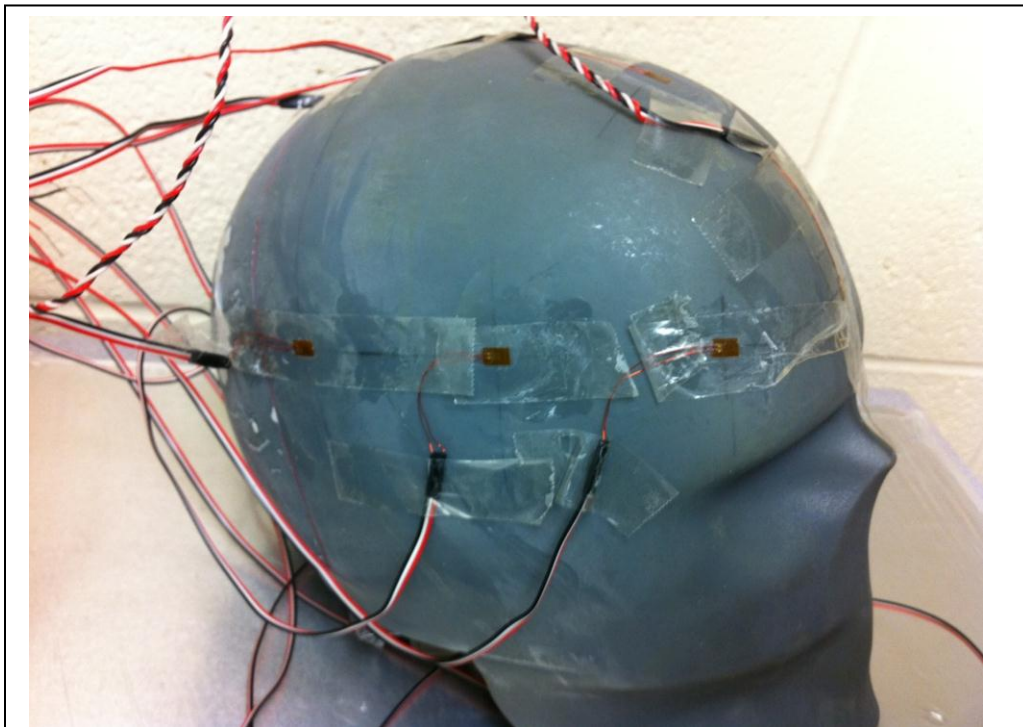


Figure 4.3.1: Strain gauge attachments on the skull of the RED Head

and the instrumentation is better achieved when the bridge circuit is completed at the gauge site (near the headform in this case) [36].

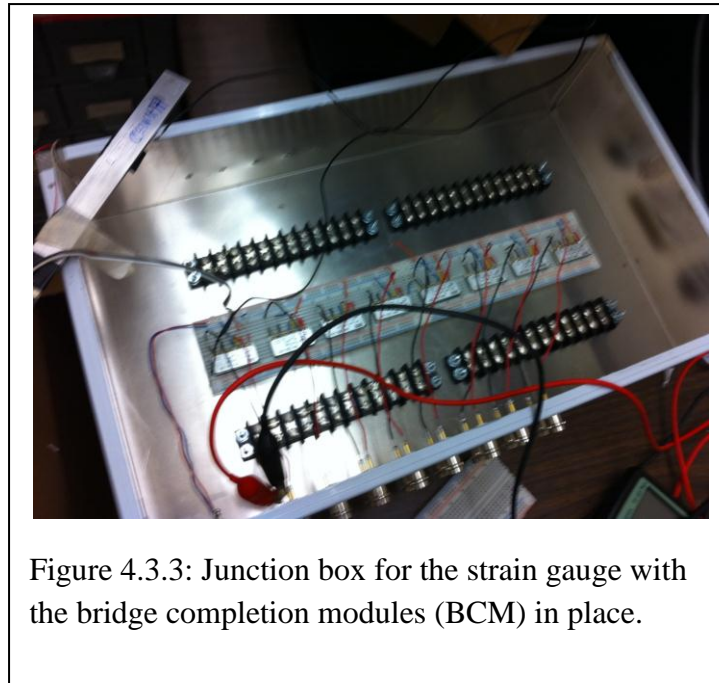
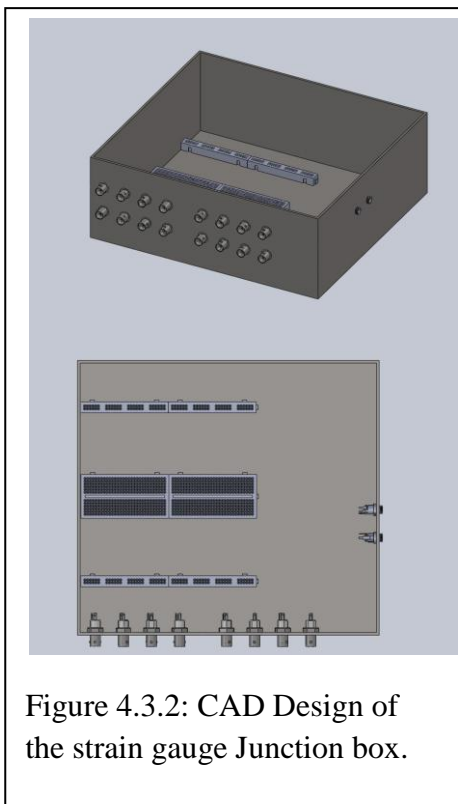
For our experiment, we chose a high resistance grid strain gauge with a Constantan foil in combination with a tough, flexible, polyimide backing, with strain range of $\pm 3\%$ and a temperature range of -100° to $+350^{\circ}\text{F}$. The gauge was applied onto the skull carefully with “M-Bond 200” adhesive, a cyanoacrylate strain gauge bond, which is widely used to produce creep free and fatigue resistance bonding.

Gauge Length	Overall Length	Grid Width	Overall Width	Matrix Length	Matrix Width	Resistance (Ohms)
0.062 in	0.114 in	0.062 in	0.062 in	0.26 in	0.15 in	350 \pm 0.15%

Table 4.1.1: Strain gauge dimensions (Source: Vishay® Micro-Measurements)

The strain gauge was powered by a Tektronix® PWS2185 power supply system and an AMETEK® Signal Recovery 5186 differential amplifier that multiplies the difference between inputs A and B by a gain factor of 10. The junction box allows the inputs into the differential amplifiers appear seamless and less cumbersome.

A junction box that houses the lead-wire system, the bridge completion modules (BCM) with power supply for excitation of the strain gauges was designed and constructed. Figures 4.3.1 and 4.3.2 shows the CAD design and the fabricated junction box with all the other materials assembled inside.



4.4: MICRO ELECTRO-MECHANICAL SYSTEMS (MEMS) ACCELEROMETERS

An accelerometer is a device that measures proper or physical acceleration, the acceleration experienced relative to a free-fall, or inertial, observer who is momentarily at rest relative to the object being measured [37].

By measuring the amount of static acceleration due to gravity, we can find out the angle the RED HEAD is tilted at with respect to the earth, and by sensing the amount of dynamic acceleration, we can analyze the way the RED HEAD is moving. The need to decouple the inertial forces happening within the brain and the head is the actual reason we needed to use an accelerometer.

To detect magnitude and direction of the acceleration as a vector quantity, single and multi-axis models can be used to sense orientation, acceleration, vibration shock, and falling [38]. In theory, an accelerometer works as a damped mass on a spring. When the

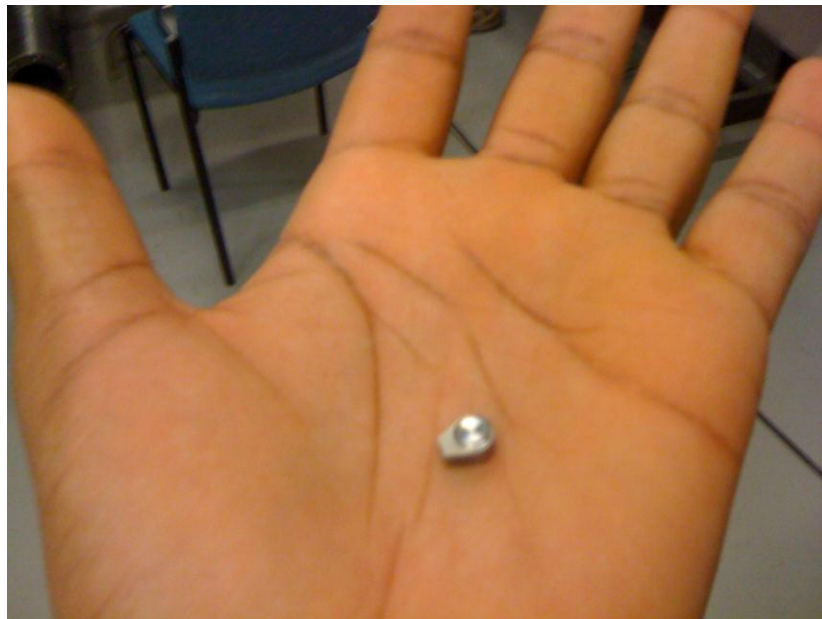


Figure 4.4: MEMS accelerometer

accelerometer experiences acceleration, the mass is displaced so that the spring is able to accelerate the mass at the same rate as the casing. The displacement is then measured to give the acceleration [38].

Some of the simplest micro electro-mechanical systems (MEMS) devices of modern times are accelerometers, consisting of little more than a cantilever with a proof mass. Damping results from the residual gas sealed in the device. As long as the Q-factor is not too low, damping does not result in a lower sensitivity [38, 39]. Q factor “*is a dimensionless parameter that compares the time constant for decay of an oscillating physical system's amplitude to its oscillation period*” and it compares the frequency at which a system oscillates to the rate at which it dissipates energy [39].

In an example of a damped mass-spring system, the Q factor is the effect of drag or viscous damping, where the damping force or drag force is proportional to velocity.

Mathematically it is written as:

$$Q = \frac{\sqrt{Mk}}{D} \quad (\text{Equation 9})$$

and defined by:

$$F_{\text{damping}} = -Dv \quad (\text{Equation 10})$$

where M is the mass, k is the spring constant, D is the damping coefficient, and v is the velocity [39].

For our experiment we chose a Dytran® **3224A** Ultra Miniature Tear Drop Accelerometer because of its miniature design, weighing only 0.2 grams, and its IEPE output. IEPE is the acronym for “*Integrated Electronics Piezo-Electric*” and defines a class of accelerometer with low impedance output and built-in electronics that works on a two-wire constant current supply with a voltage output on a DC voltage bias. IEPE two-wire accelerometers are easy to install, have a wide frequency response, can run over long cable lengths and are relatively cheap to purchase. The IEPE technology has generally replaced most 3-wire accelerometers and is broadly used for most applications except for specialist applications such as zero-Hz accelerometers, high-temperature applications or 4-20mA accelerometers used in the process industries [40].

The accelerometer is a digital type with a capacitive silicon micro machined sensing element that serves as the small cantilever. The cantilever is located inside the cavity of a small silicon block. The elastic property of silicon is the basis of the acceleration sensing. Other reason we chose this type are the axis type, sensitivity, bandwidth and maximum swing.

4.5: FIBER OPTIC SENSOR

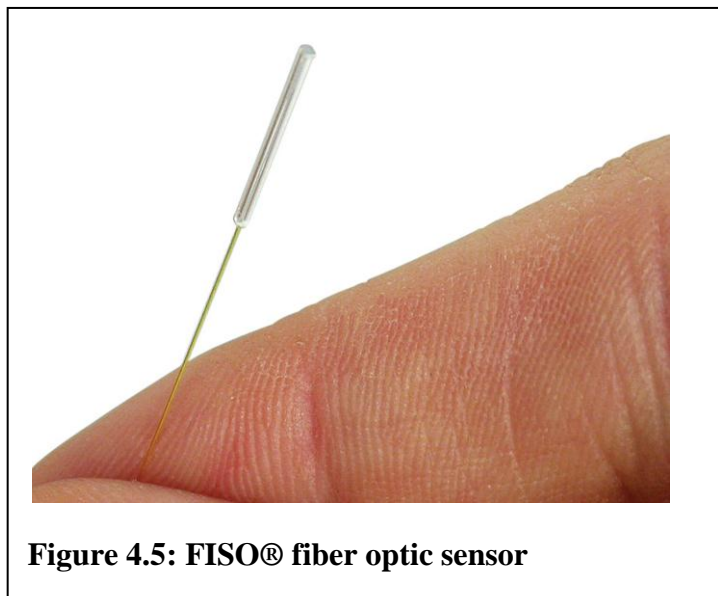
With a diameter of only 125 μm , the FISO® Technologies FOP-F125 is perhaps the smallest pressure sensor commercially available. This ultra-miniature sensor is manufactured directly at the tip of the optical fiber, and the all-glass sensor is fully biocompatible [2]. The size and mounting flexibility of the sensor provides the capability to embed the sensor within our surrogate brain. The sensor allows in-situ measurements at locations unreachable to many standard pressure sensors and eliminates the artifacts

due to material contact that may be encountered with laterally mounted sensors such as a PVDF that has to be properly orientated to get good and useful pressure measurements [41].

Orientation of the fiber optic sensor has no bearing on the pressure measurement to be taken, as in the case of its placement within the brain surrogate, only the sensor position is needed to detect the wave propagation within the material.

The sensors' high measurement resolution and precision, combined with a fast reading rate, are important characteristics when attempting to detect very quick and subtle pressure variations as with blast wave mechanics. It allows a clear definition of complex pressure waveforms, such as those generated within the event(s) producing brain injury. Its long term reliability and low drift value make it the best sensor available for implantable equipment, such as intra-cranial, intravascular and intrauterine pressure monitoring devices [41].

The optical nature of the sensor makes it immune to electromagnetic field or radiofrequency interferences [41]. They have also been demonstrated to function inside a



liquid, which is extremely useful in detecting pressure attenuation in cerebrospinal fluid (CSF) [42].

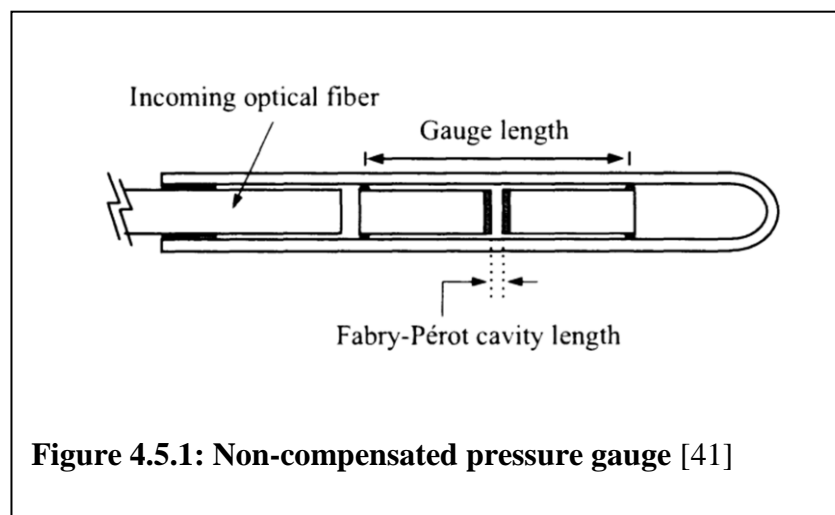
4.5.1: FABRY-PÉROT FIBER OPTIC GAUGES

FISO® Technologies' fiber optic gauges are based on the Fabry-Pérot interferometer (FPI). An FPI consists of two mirrors facing each other. The space separating the mirrors is called the cavity length. Light reflected from the FPI is wavelength-modulated in exact accordance with the cavity length [41, 43].

From Figure 4.5.1, the Fabry-Pérot cavity contains mirrors on the tips of the two multimode optical fibers inserted inside a micro-capillary. During its application, the strain transferred from the specimen to the gauge can be deduced from the difference in the cavity-length; the strain is calculated according to the following equation:

$$\text{Strain} = \Delta L_{\text{Cavity}}/L_{\text{Gauge}} \quad (\text{Equation 11})$$

where ΔL_{Cavity} is the variation of the cavity length and L_{Gauge} is the gauge length, i.e. the distance separating the spots where the optical fibers are welded to the micro-capillary [41].



It is important to note that the “*long-term reliability of the gauge length is guaranteed by the quartz-to-quartz welding method which avoids any creep*” [41]. The sensing part of the gauge is located within the gauge length area and the sensitivity of the gauge has been determined during manufacture by varying the gauge length, which is also defined as the scale factor. The FISO® Veloce signal conditioner can measure and interpret the cavity length with a resolution of 5 nm [41].

The cavity length of FISO®’s fiber optic sensors and the pressure measurement data taken by it are “*insensitive to any pulling or manipulation of the incoming fiber*” because the incoming optical fiber which brings light to the gauge is mechanically decoupled from the sensor’s sensitive optical fibers [41].

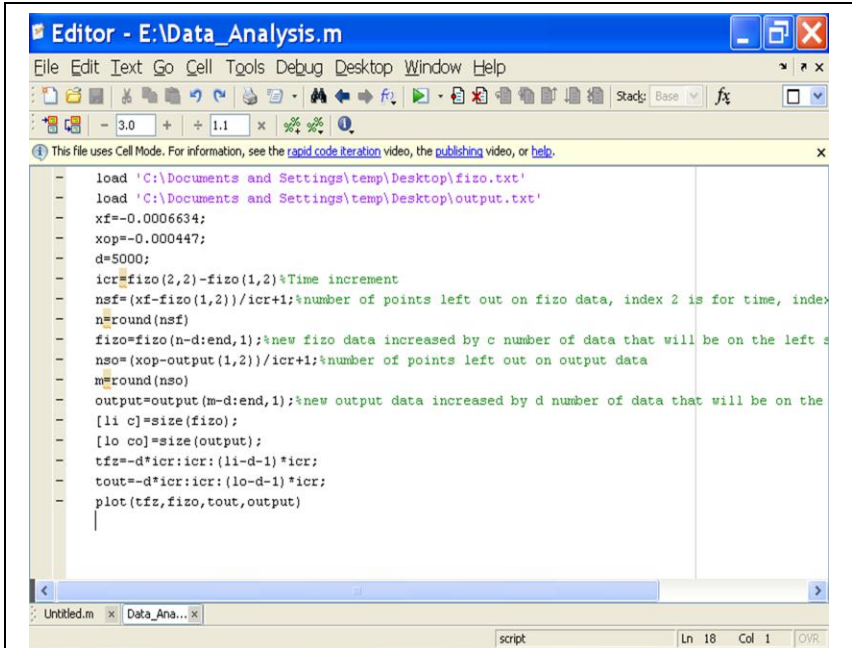
Sensor	FISO	PVDF
Size	125µm	1mm
Material	Fiber optic	Polymer
Hysteresis	No	Yes
Wavelength modulated	Yes	No
Sensitivity	High	Low
Noise	Low	High
Output	Voltage	Electric Charge
Accuracy	High	Low
Temperature range	>> 90°	90°
Measurement	Local, directional	Uni-axial
Geometry	Small, and round	Bulky

Table 4.5.1: Fiber optic gauge vs. PVDF gauge

4.6: DATA ACQUISITION SYSTEM

This section is divided into two parts, namely, software and hardware. The software programs used are Matlab® (matrix laboratory), a numerical computing environment and programming language that allows matrix manipulations, plotting of functions and data, and implementation of algorithms, and National Instruments LabVIEW® RT server and LabVIEW® 2009. Fig. 4.6 shows a sample of the program written in Matlab® specifically for interpretation and analysis of the data retrieved from the data acquisition software.

LabVIEW® is a platform and development environment for visual programming language. It is a data flow/graphical programming language and also referred to as G. Working with LabView® makes it easier to create a data acquisition application graphically with virtual instruments (VI). This VIs are dragged and dropped on to the



```

- load 'C:\Documents and Settings\temp\Desktop\fizo.txt'
- load 'C:\Documents and Settings\temp\Desktop\output.txt'
xf=-0.0006634;
xop=-0.000447;
d=5000;
icr=fizo(2,2)-fizo(1,2)*Time increment
nsf=(xf-fizo(1,2))/icr+1;%number of points left out on fizo data, index 2 is for time, index
n=round(nsf)
fizo=fizo(n-d:end,1);%new fizo data increased by c number of data that will be on the left s
nso=(xop-output(1,2))/icr+1;%number of points left out on output data
m=round(nso)
output=output(m-d:end,1);%new output data increased by d number of data that will be on the
[li c]=size(fizo);
[lo co]=size(output);
tfz=d*icr:icr:(li-d-1)*icr;
tout=d*icr:icr:(lo-d-1)*icr;
plot(tfz,fizo,tout,output)

```

Figure 4.6: A screen capture of the Matlab® software used in data processing.

front panel of the software to form a system of block diagrams connected with drawing wires that can be then be executed.

The reason why we chose to go with a LabVIEW® Real Time OS as an alternative to Microsoft® Windows-based systems is because a real-time software architecture is useful for time-critical applications requiring deterministic loop rates and headless operation, especially as in blast wave attenuation detection since the whole process happens in such a short amount of time. Real-time operating systems help to prioritize tasks so that the most critical task always takes control of the processor when needed. With this feature, an application can run with predictable results and reduce jitter [44].

4.6.1: HARDWARE

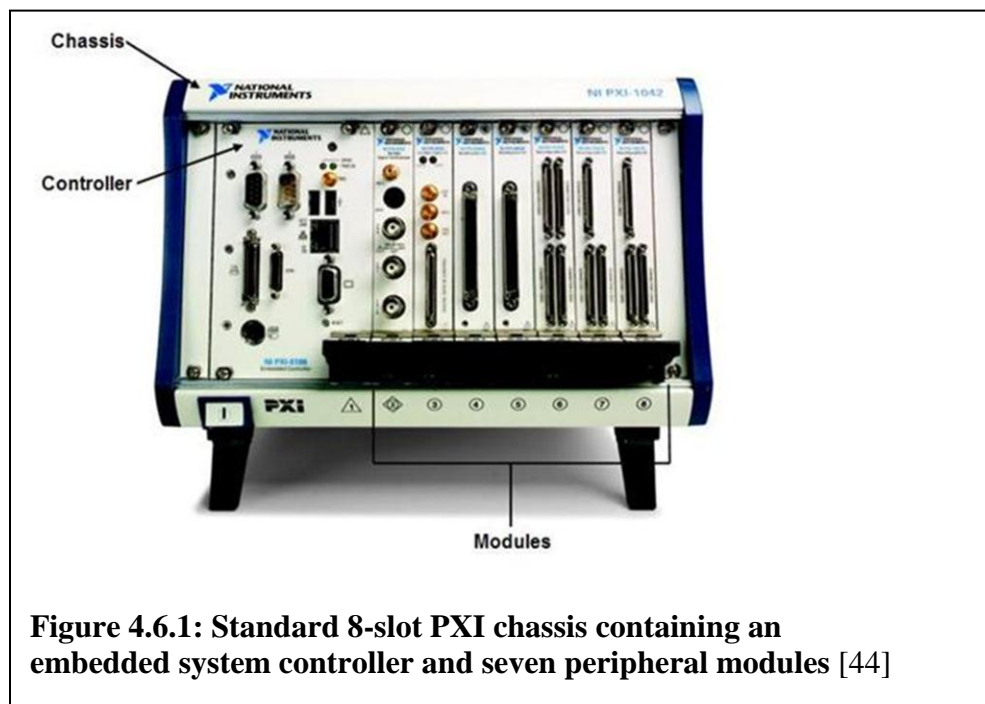
The Veloce system is a high speed and universal fiber optic signal conditioner that can be used to measure relative strain, temperature, force and load, and pressure in difficult locations that may be unreachable with other measuring instruments. The conditioner has a sampling rate of 200 kHz and is best suited for applications that require dynamic readings and fast response time [41].

The other hardware specifically selected as part of the data acquisition system is the National Instruments PXI platform. PCI eXtensions for Instrumentation (PXI) is a modular instrumentation platform originally introduced in 1997 by National Instruments, Inc. It is designed for measurement and automation applications that require high performance and a rugged industrial form factor. PXI has many applications including

test and measurement, and data acquisition which are the main reasons we chose to go with this kind of hardware.

The PXI system has three other components, and as shown in Figure 4.6.1, they are the chassis, system controller and peripheral modules.

The main reason we chose this system is because it has PCI Multifunction Data Acquisition (DAQ) boards that can capture data at up to 250 kS/s, with 4 analog output channels and up to 32 analog input channels, and with the help of LabVIEW® Real-Time the data are buffered locally and can be written directly to an on-board hard drive, without any interference or any control from an outside source. The two DAQs used are NI PCI-6220. The chassis of the PXI system is very rugged and it allows for multiple PXI system configurations to meet our data acquisition needs.



The embedded controllers eliminate the need for an external PC; therefore they serve as a complete system contained within the PXI chassis. There was also no need to plug extra peripherals into this unit because the embedded controllers come with standard features such as an integrated CPU, hard drive, RAM, Ethernet, USB, and other peripherals, as well as LabVIEW® Real-Time OS and all Microsoft Windows device drivers already installed.

We were able to control The PXI system from a standalone desktop computer running Microsoft® Windows OS through a software- and driver-transparent link. During boot-up, the computer recognizes all peripheral modules in the PXI system as PCI boards, and you can then work with these devices through the controller [44].

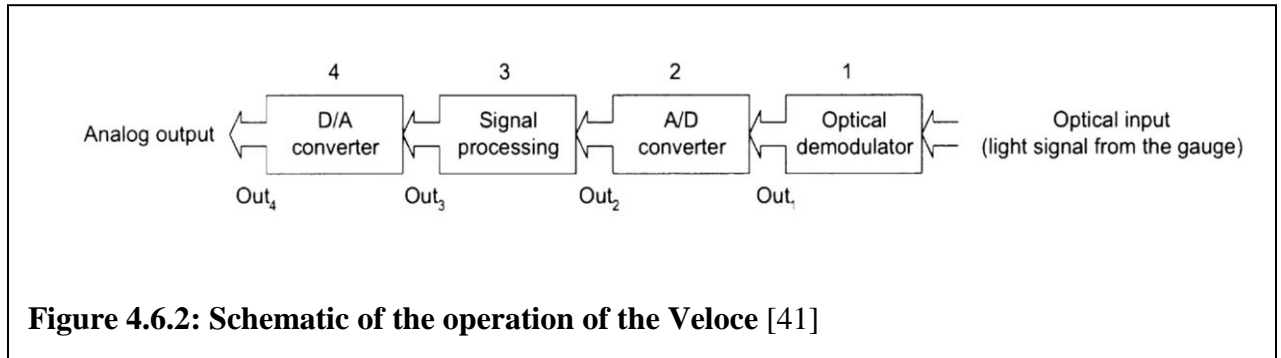
4.6.2: PRINCIPLE OF THE VELOCE SIGNAL CONDITIONER

A light signal from the gauge is fed as input into the optical demodulator. The analog output signal of the demodulator Out_1 is then converted to digital signal by the analog-to-digital converter at a sampling rate of 200 kHz. The digital output signal Out_2 is then passed to the digital signal processor (DSP). The digital output signal Out_3 is then converted back again to analog signal by the digital-to-analog converter and then send to the analog output [41].

The signal coming out of the optical demodulator, Out_1 , is a sinusoidal function of the time-dependent cavity length of the gauge, given mathematically as:

$$Out_1(t) = A \times \sin [2\pi \times L_{Cavity}(t) / VSF] \quad (\text{Equation 12})$$

where A is the amplitude of the signal or the A factor and VSF is the Veloce Scale Factor and ranges from 420 nm to 430 nm. Both A and VSF are constants which are characteristics of the conditioner. 1 mV at the analog output always corresponds to 2 nm of gauge cavity length [41].



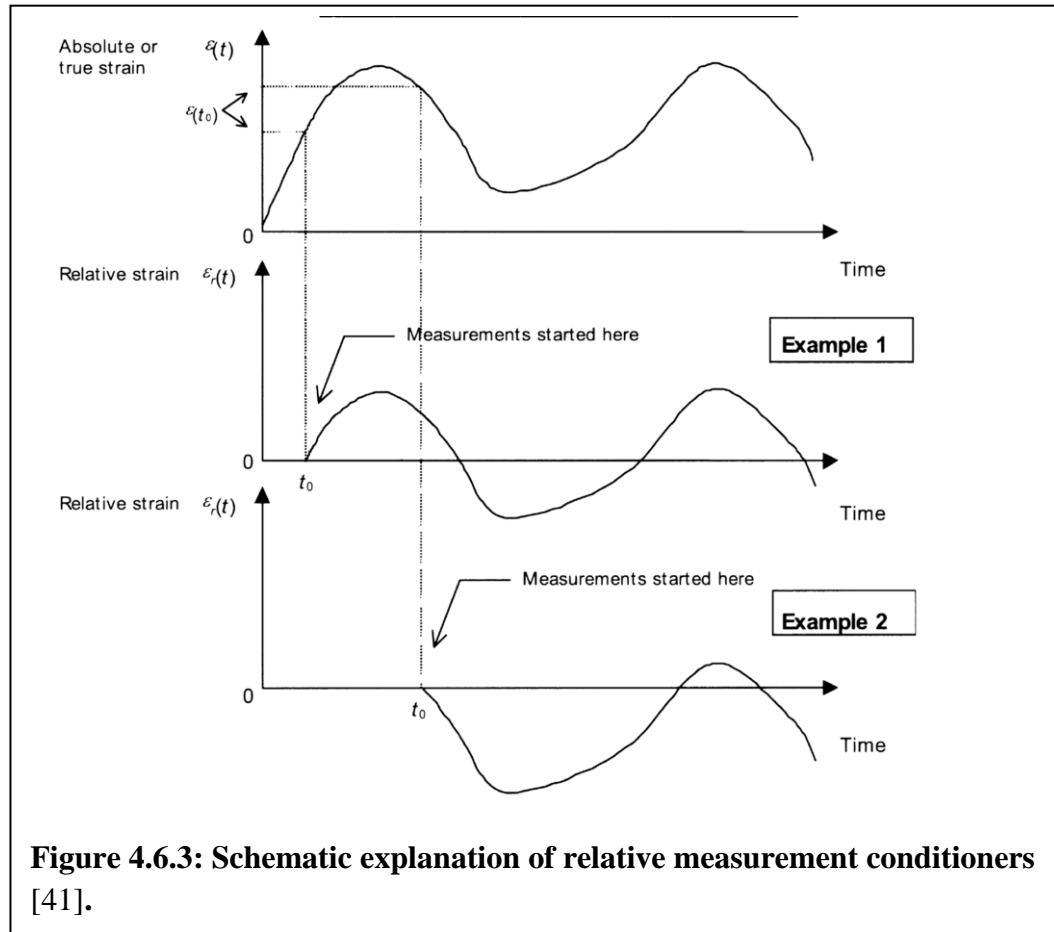
The gauge cavity length L_{Cavity} can be read by the conditioner between 13 μm to 19 μm , or 13000 nm to 19000 nm. Beyond this range, the amplitude of the signal (the A factor) becomes too small to get an accurate calculations [41].

Equation (11) shows that the maximum frequency of Out_1 is proportional to the rate of change of the cavity length. The maximum change of the cavity length between the two samples of the A/D converter cannot exceed one half of the VSF, that is, 200 nm per sampling interval [41]. The frequency bandwidth of the Veloce signal conditioner is mostly limited by the incoming signal, but, for small signals of maximum excursion that is lower than $\text{VSF}/2$, the signal bandwidth is limited to the Nyquist stability criterion of half of the sampling rate of the Veloce system (i.e. 100 kHz) [41, 45].

4.6.3: RELATIVE CONDITIONER VERSUS ABSOLUTE CONDITIONER

One of the reasons why we chose the FISO® fiber-optic conditioner is because it is an absolute measurement conditioner as opposed to relative measurement conditioners. In an absolute conditioner the measurement from the data readings are absolute or true measurement values of the physical stimulus (pressure, etc.) while the data readings of a relative measurement conditioner are values relative to an initial or referenced value of the physical stimulus [41]. One important thing to note is that, there is no loss of the true reference (or initial state) of the sensors when the conditioner is turned OFF or reset.

Figure 4.6.3 shows the advantages of using a relative measurement conditioner. The first graph of the figure shows the absolute or true values versus time measured by an absolute measurement conditioner. The second graph of the figure or example 1 shows the values measured using a relative measurement conditioner started at an initial time t_0 (i.e. t_0 is the time at which the conditioner is tuned on or is reset). The graph in example 2 is the same as example 1 except that the measurements are started at a different initial time t_0 . In both examples 1 and 2 the measured values are relative to the initial value of the transducer at time t_0 but because the initial state of the transducer is different at these two times, the relative value will be different [41].



The relative value is expressed mathematically as:

$$\varepsilon_r(t) = \varepsilon(t) - \varepsilon(t_0) \quad (\text{Equation 13})$$

where: $\varepsilon_r(t)$ is the relative value as function of time

$\varepsilon(t)$ is the absolute or true value as function of time

$\varepsilon(t_0)$ is the absolute or true value at time t_0

4.7: CALIBRATION

For the purpose of maintaining and ensuring accuracy of data, the instruments including the sensors have to be calibrated. According to Dahlberg [46] calibration is a process that provides information so that adequate adjustments can be made if required on a test or the transducer [46]. Two fiber optic sensors; *FISO*® 1010032208 and *FISO*® 1010032209 were picked from the lot of 10. Three experiments were designed for the calibration test. Specimen preparation as shown in Figure 4.7.2 was designed and fabricated to be used for the experiments. The first one was a static test with the MTS machine, where a set of loads was applied gradually to the Jell-O specimen with the sensors inserted into the Jell-O and the result compared with the standardized results from the manufacturer. The results from the static tests were unreliable, the error ranges were so high from the manufacturer's figures and with no direct interpretation, and this is due to the fact that the sensors were more of a dynamic sensor than static.

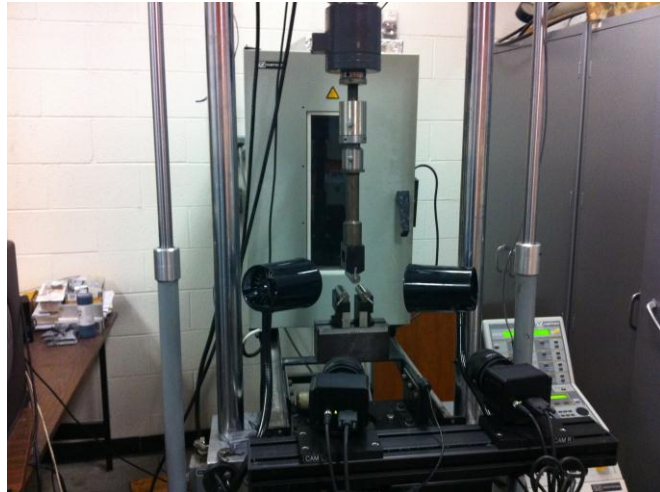


Figure 4.7: The MTS machine

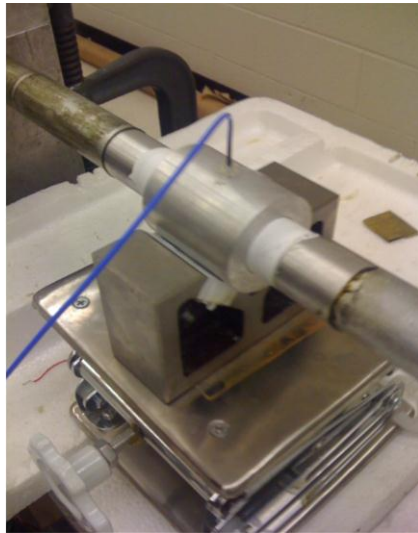


Figure 4.7.1: Kolsky bar test set up

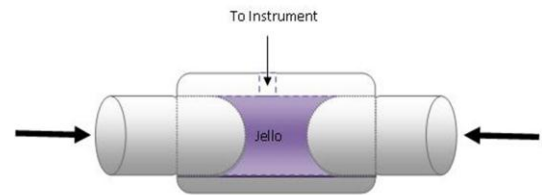


Figure 4.7.2: Calibration test with the pressure sensor embedded in a Jell-O material.

The second one was the Kolsky pressure bar test, where measured pressure from the test was compared with the manufacturer's figures shown below in Tables 4.7.1 and 4.7.2; a total of two tests were conducted using two equal elastic bars with the sensors inserted in a gel medium between their ends so as to generate an elastic (pressure) wave through a shock from one of the ends, which travels along the bars.

Pressure (psi)	Cavity Length (nm)	Measured Pressure (psi)	Error (%)
15	18268	14.49	0.34
105	16691.4	105.51	-0.34
135	16180.7	134.99	0

Table 4.7.1: Calibration report of FISO® 1010032209 fiber optic sensor with gauge factor 6011732 and sensitivity of 17.32nm/psi

Pressure (psi)	Cavity Length (nm)	Measured Pressure (psi)	Error (%)
15	18231.4	14.35	0.43
105	16672.9	105.52	-0.35
135	16167.6	135.08	-0.05

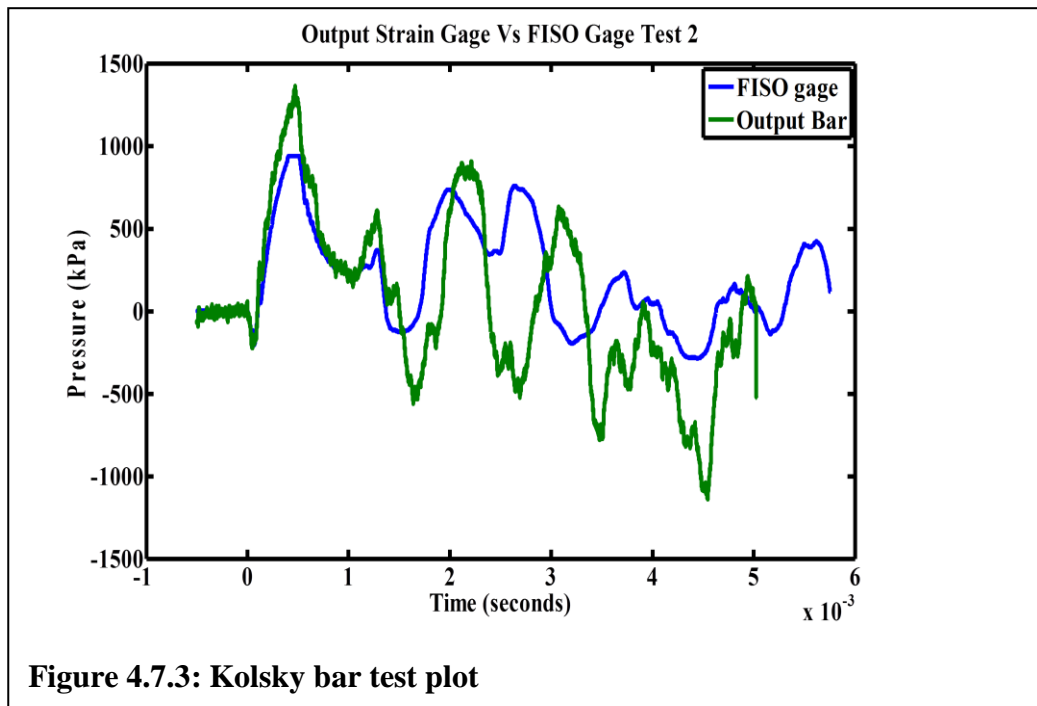
Table 4.7.2: Calibration report of FISO® 1010032208 fiber optic sensor with gauge factor 6011710 and sensitivity of 17.10nm/psi

The result as shown in Figure 4.7.3 is a comparison of the fiber optic sensor in the specimen and the output strain gauge. The results were converted to pressure based on the following known mathematical equation:

$$\text{Result}_{\text{psi}} = \text{Analog}_{\text{mV}} * \text{Scale Factor}_{\text{psi/mV}} + \text{Offset}_{\text{psi}} \quad (\text{Equation 14})$$

where $\text{Analog}_{\text{mV}}$ = the pressure reading in millivolts, $\text{Scale Factor}_{\text{psi/mV}} = 0.030006 \times 10^3$, and $\text{Offset}_{\text{psi}}$ is a constant and equal to -0.0564. These values are independent and vary with each sensor. Note that 1 psi = 6.895 kPa.

It could be noted from the plot that the fiber optic sensor maxed out at 1000 kPa and we were able to verify that with the manufacturer's proportionality constant.



The accuracy of the FISO® sensors claimed by the manufacturer is given in Tables 4.7.1 and 4.7.2. To verify the level of trust in these sensor readings in a less controlled environment more characteristic of our shock system, comparative readings were taken using a Kolsky bar apparatus, using strain gauges on the bars to compare against the FISO® readings. The average percentage error from the Kolsky bar

calibration was calculated based on peak values in Figure 4.7.3. It should be noted that the error from 0 to 1 ms is a bit stable but that value begins to deviate as the duration prolongs from 1.5 ms to 3 ms, making the FISO® sensors to drift and hence the measurements become error prone. The FISO® sensors can be trusted for accurate reading within about 1-2 ms time frame after which there is a gradual voltage drop and the measurements become suspect due to the high error rate. The average percentage error was picked from several pressure values from the set prior to 3 ms and the percentage error calculated for each time domain and then an average percentage error of the entire system was calculated (see Table 4.7.3).

	Peak 1		Peak 2		Peak 3	
FISO	400 kPa	1.4 ms	800 kPa	2 ms	820 kPa	2.85 ms
OUTPUT	580 kPa	1.4 ms	915 kPa	2.3 ms	610 kPa	3.1 ms
ERROR/Δt	-0.31	0	-0.12	0.3 ms	0.34	-0.25 ms

Table 4.7.3: Error table from the Kolsky bar test - FISO® vs. output bar gauge

The third set up, as shown in Figure 4.7.4, is the cylinder shock-tube test, using a small polycarbonate cylinder, filled with silicone gel and with a cross-section area 1/10 of the shock tube area, with the sensors embedded.

To create the cylinder, the thickness was calculated to have similar flexural stiffness to skull, using real properties from the human skull, which from literature has different values based on the part of the skull that is been examined but with an average Young's modulus E of 5370N/mm² and diameter of 150mm, and compared to that of an Amorphous polycarbonate material that serves as the cylinder material and is given as follows:

	Young's Modulus (E)	Diameter (d)	Thickness (t)
<u>Skull</u>	5370N/mm ²	150mm	6.9mm
<u>Cylinder (Amorphous Polycarbonate)</u>	2380N/mm ²	22.8mm	

Table 4.7.4: Mechanical properties comparison for cylinder test design

$$\left(\frac{d^3}{E*t^3}\right)_{skull} = \left(\frac{d^3}{E*t^3}\right)_{cylinder} \quad (\text{Equation 15})$$

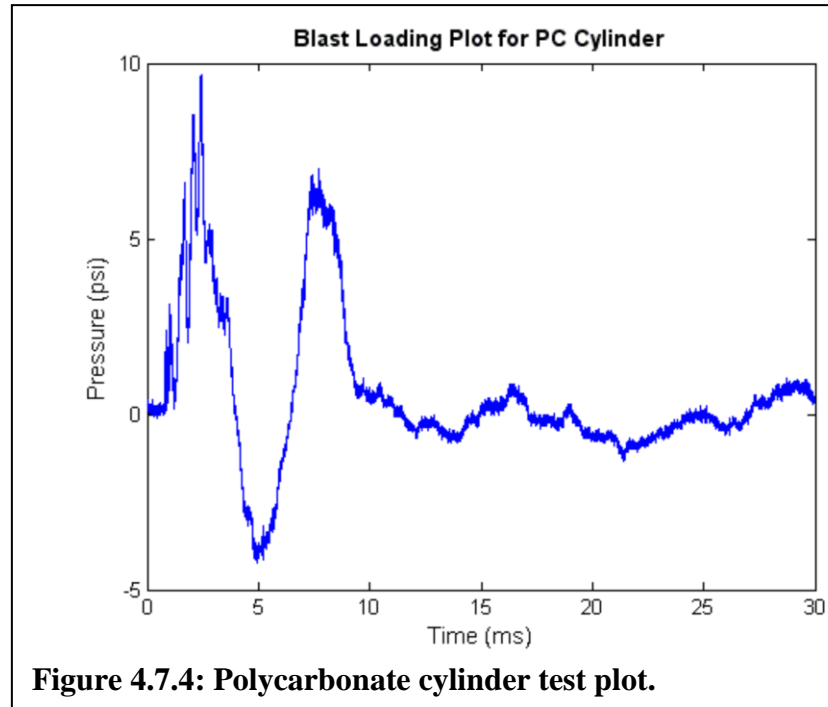
$$\left(\frac{d^3}{E*t^3}\right) = \left(\frac{d^3}{E*t^3}\right) \quad (\text{Equation 16})$$

$$\left(\frac{150^3}{5370*6.9t^3}\right) = \left(\frac{22.86^3}{2380*t^3}\right) \quad (\text{Equation 17})$$

$$1.9 = \left(\frac{5.02}{t^3}\right) \quad (\text{Equation 18})$$

$$t = 1.379218797\text{ms}$$

(Equation 19)



We also made sure that the strain gauge was working and performed some basic bending tests to make sure the junction box was responding. We also calibrated the bridge completion modules (BCMs) individually to make sure that the amount of electricity put in is what we are outputting.

Calibration of the data acquisition system helps to assess the sources of measurement error. It also helps in the selection process of the most appropriate instrument to use. A quality control strategy was formulated to ensure that only properly calibrated instruments and sensors will be used during the tests and that all measurement errors are identified, quantified, and compensated for [47].

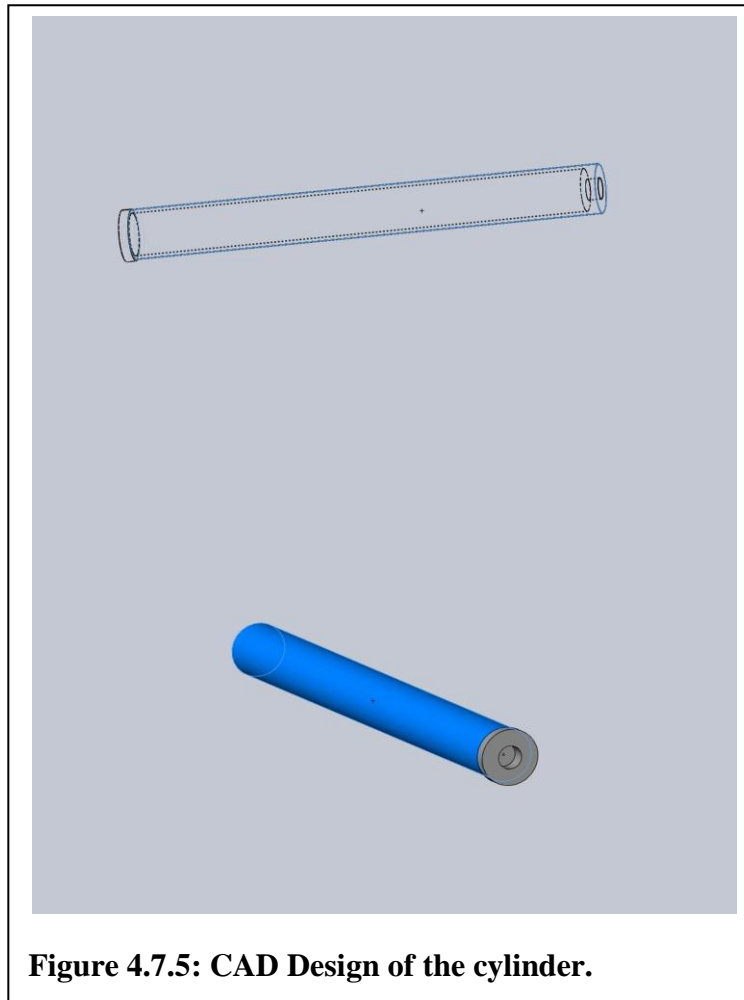


Figure 4.7.5: CAD Design of the cylinder.

As shown in Figure 4.7.6, to calibrate the BCMs (E), we attached a strain gauge to an aluminum rod, and connected it to the signal conditioner (D) and then to the input of the junction box (A). A power supply (B), not lower than 5 V and not exceeding 12 V was then used to power the junction box (A) and ultimately the BCMs (E).

When the aluminum undergoes a specified deformation, the DAQ (C) displays the corresponding action graphically. These results are then checked mathematically and compared to the measured signal.

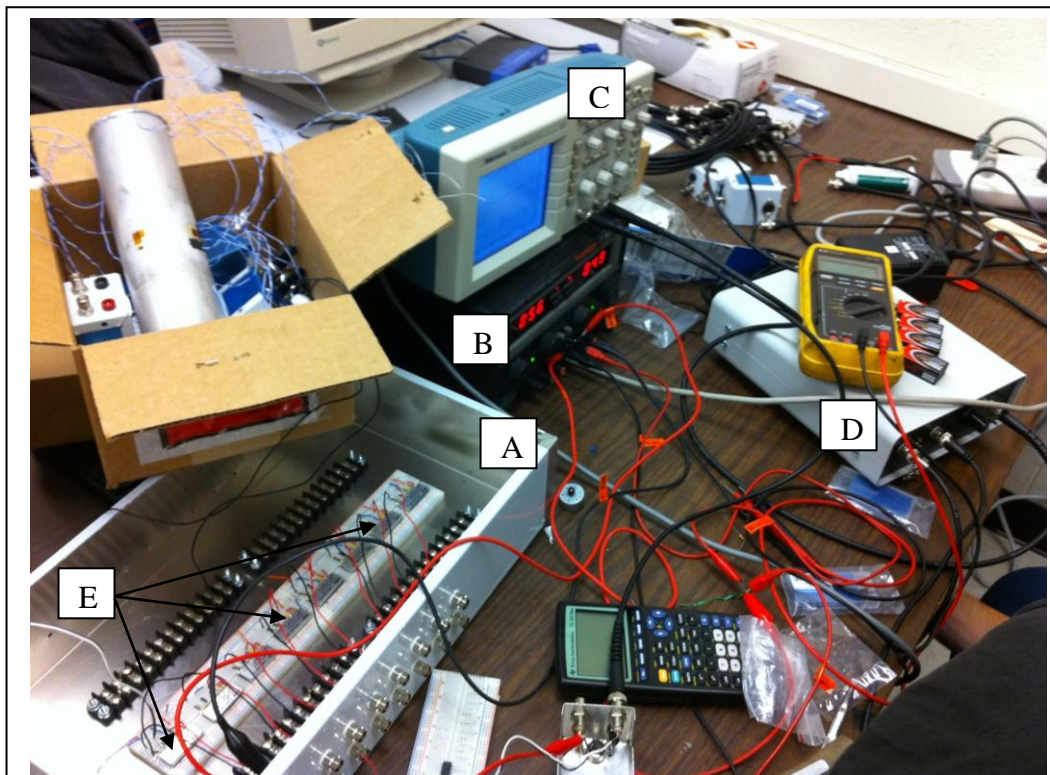


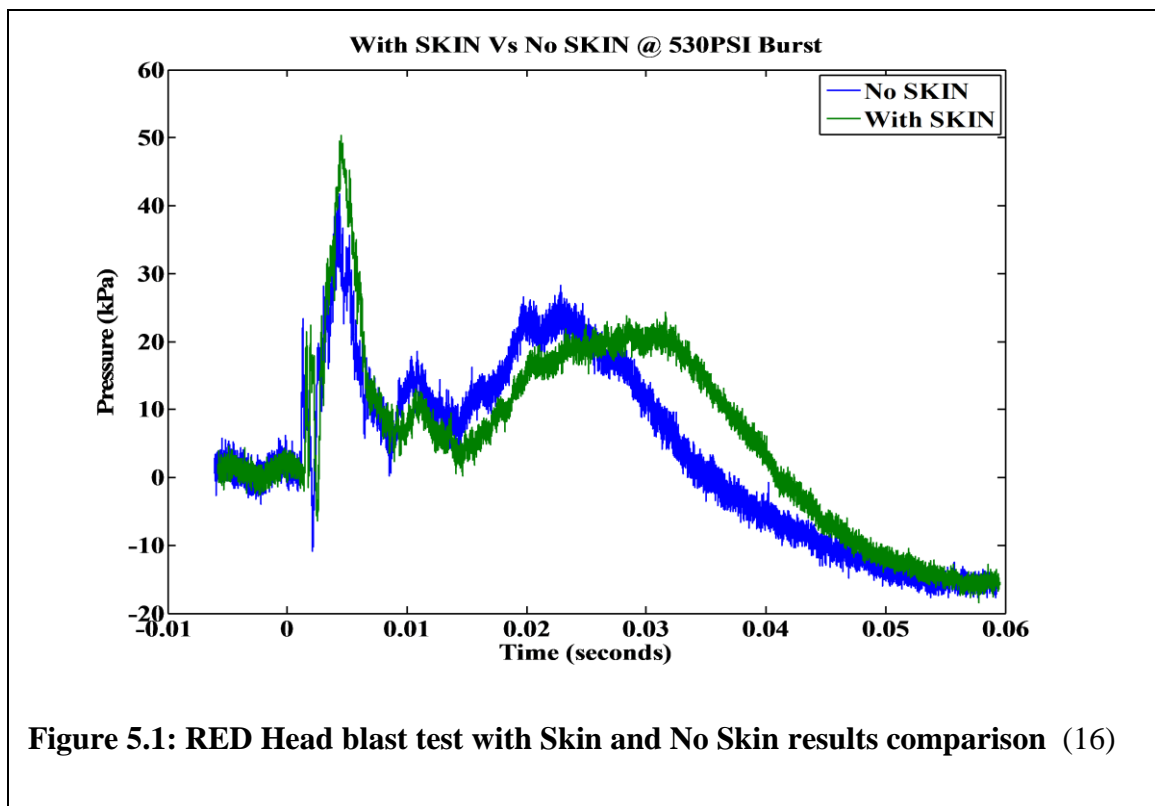
Figure 4.7.6: The setup for calibrating the bridge completion modules (BCM).

Chapter 5: Results and Analysis

5.1: INITIAL TEST

Two initial shock tests were performed with the RED Head. Each test had the FISO® pressure gauges inserted into the surrogate brain. The aim of the test was to find the overpressure in the brain with or without the PDMS skin on the RED Head.

At approximately the same breech pressure, the overpressure in the RED Head with skin was 48.92kPa and 41.74kPa with no skin. Because the PDMS skin was not properly laminated to the skull, a pressure buildup was noticed in the “*With Skin*” experiment confirming earlier report(s) on pressure build-ups in and around the head with



the presence of a helmet [48]. However, more tests need to be done to confirm this phenomenon. The secondary overpressure in the “*No Skin*” test was 27.69KPa and 23.61kPa “*With Skin*.” Due to the skin delamination, future experiments were modeled along the “*No Skin*” RED Head test design to make measurements more repeatable.

5.2: TEST/EXPERIMENT DESIGN

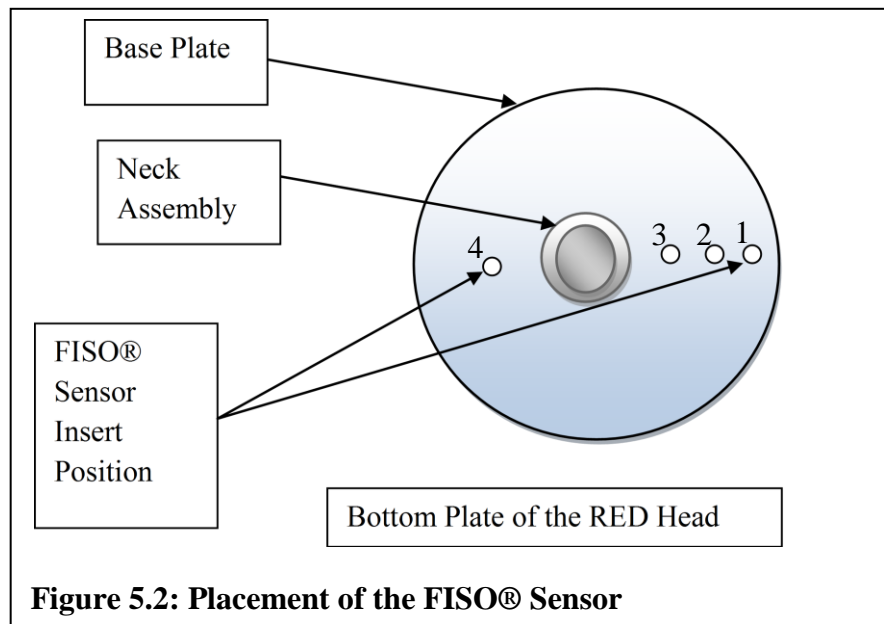
The RED Head was prepared with a surrogate brain, and instrumented as previously described. The aim of the test is to study the propagation of blast wave and its attenuation along the experimental headform and in the simulated brain. The brain is simulated with a silicone gel, the CSF is not simulated in this experiment due to the likelihood of formation of vapor bubbles because of the low vapor pressure or cavitation that can be experienced in water in tight cylindrical tube, and the meninges, a membrane that envelopes the brain, is simulated in its place by a polyethylene plastic bag.

Since attenuation is an exponential function of the path length of the blast waves through the brain simulant, we hope to see a gradual loss in intensity of the pressure/blast waves as they propagate through the skull, the meninges and into the simulated brain, and as attenuation affects the propagation of the pressure waves, we hope to see a reduction in amplitude in the pressure wave profile.

The experimental approach is divided into two parts; the first part is the test for the propagation of blast waves through the surrogate headform only, where we hope to see the strain on the surface of the headform, and the second part is the test for the

propagation of blast wave through the headform into the brain simulant, where we hope to characterize pressure waves inside the surrogate brain.

The schematic of the experimental approach is shown in Figure 4.1 and the arrangement of sensors inside the headform is shown below in Figure 5.2. The sensors are carefully placed and marked on the base plate before insertion, and an existing hole was placed on the base plate. The surrogate brain had dummy sensors place in them while curing so as to allow the placement of the fiber optic sensors later. From Figure 5.3 the FISO® sensor is placed 3 inches inside the surrogate brain from the bottom plate of the RED Head, while the RED Head is placed 5 inches away from the exit of the shock tube and is well bolted down to the neck assembly, which in turn is bolted down to the RED Head stand.



There are ten strain gauges and they are arranged as shown in Figure 5.2.1. Gauges 1, 2, 10 and 8 are arranged laterally while 3, 4, 5, 6, 7 are arranged vertically. Gauge 9 is attached opposite of gauge 1 and laterally inside the skull around the curvature.

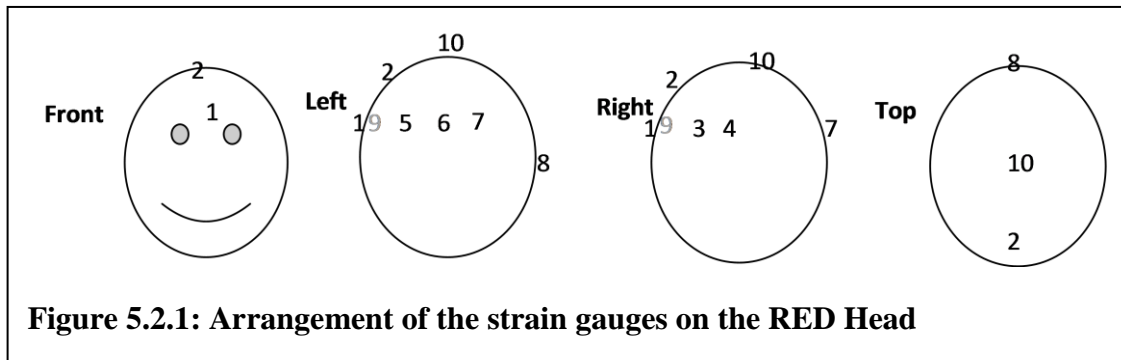


Figure 5.2.1: Arrangement of the strain gauges on the RED Head

5.3: METHODS

The setup of the experiment consists of (a) the shockwave generator/shock tube, (b) the instrumented headform with four FISO® pressure sensors and ten strain gauges arranged as shown in Figures 5.2.1 and 5.3 respectively. There is also a ninth strain gauge (number 9) inside the skull cavity adjacent to gauge number 1. The configuration of the gauges within the headform and the simulant is to allow us to detect the gradual propagation of the pressure waves through the headform and into/through the brain simulant. The positioning is purposefully based on earlier modeling by Ganpule [48] that predicts the most optimal position to place the gauges.

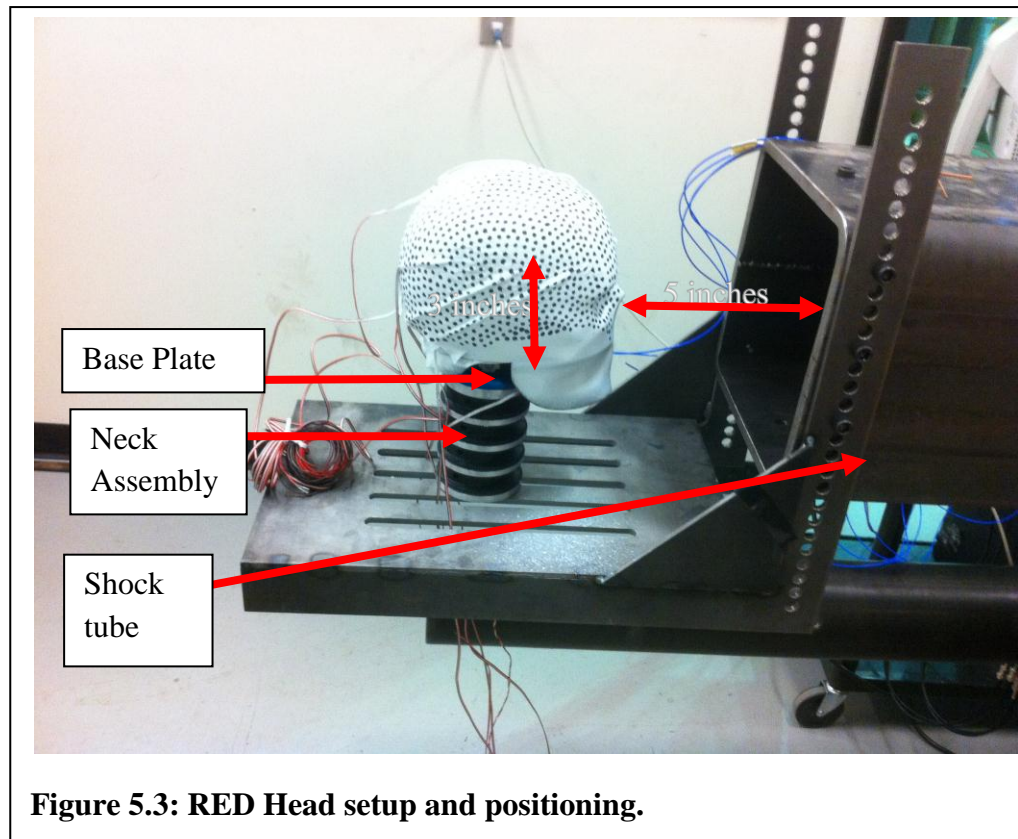


Figure 5.3: RED Head setup and positioning.

The position of the headform in relation to the shockwave generator is shown in Figure 5.3. The blast will emanate from the shockwave generator when the membrane in the shock tube (Figure 5.3.3) that separates a high pressure “driving” gas from ambient “driven” gas ruptures, causing a temperature and pressure increase in the tube, and ultimately generating a shockwave that moves through the tube and to the headform which is at the outflow end of the tube. The pressure is controlled and achieved through the adjustable volume breech and the membrane holder by varying the membrane (MYLAR®) thicknesses and quantities to obtain different blast amplitudes.

When the blast hits the headform, the measurement is made possible by the use of the FISO® fiber optic sensors and the strain gauges. The data acquisition setup is shown in Figures 5.3. and 5.3.2. It comprises (a) a National Instruments PXI, (b) a FISO® Veloce signal conditioner for the FISO® sensors, (c) a signal charge amplifier for the strain gauges, and (d) a computer system with independent display unit. The computer system runs LabVIEW 2009 programming software that controls the entire data acquisition system setup and displays the captured data in graphical form. The PXI, however, is a standalone data acquisition unit running a LabVIEW Real-Time OS.



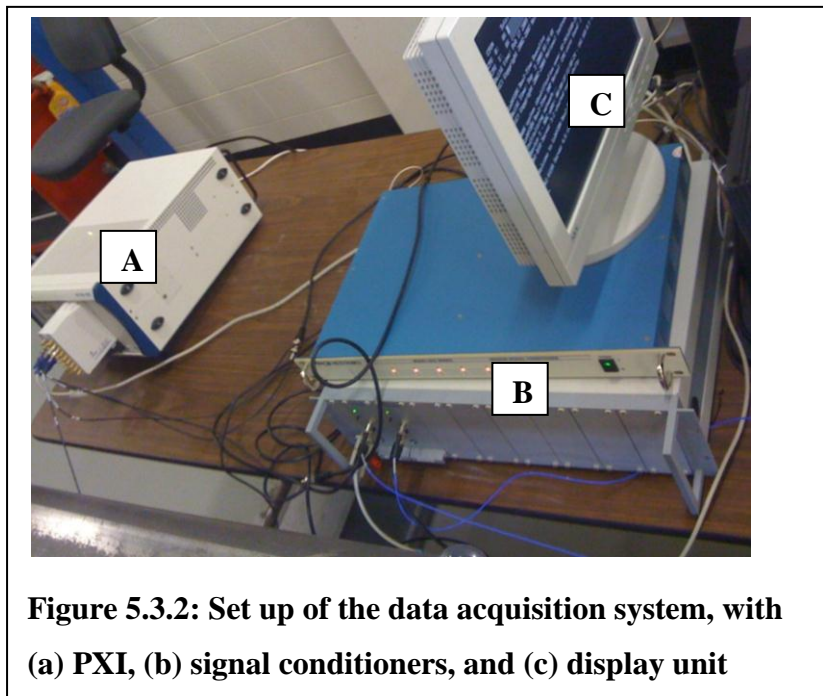
Figure 5.3.1: Part of the data acquisition system set up for the strain gages, this include the junction box, signal amplifiers, power supply and a DAQ.

The experiment includes 11 shots ranging from the lowest membrane thickness of 0.01 inches to the highest of 0.1 inches to produce a breech pressure between 92 PSI and

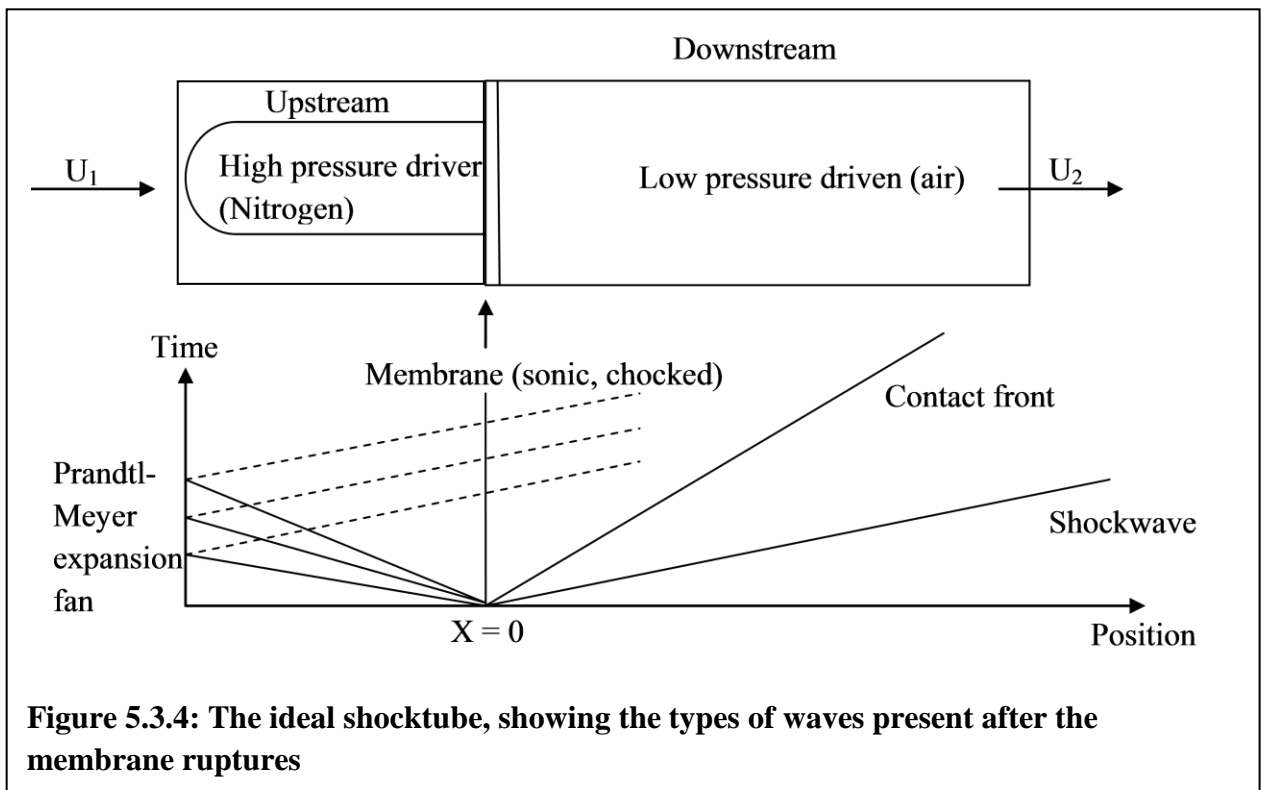
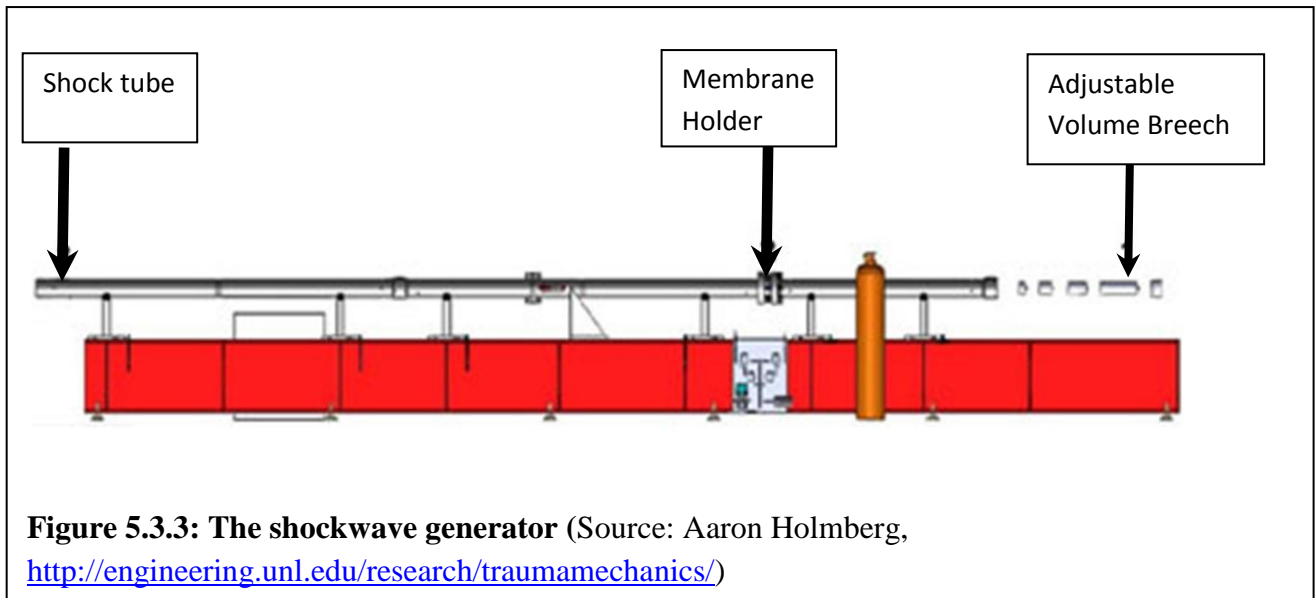
1219 PSI. Tests of burst pressures of 500 to 600 PSI and those above 1000 PSI were repeated for comparison.

The shock tube is prepared, the nitrogen driver gas is pumped into the shocktube breech, and a pressure P_1 builds up and is held back by the membrane with thickness t in the upstream. After the membrane ruptures, a shock with speed U_1 develops and flows through the shock front towards the downstream and emerges as U_2 . After the RED Head experiences shock, a back flow or rarefaction wave (Prandtl-Meyer expansion wave) moving in the same direction as the shock is then observed with speed U_b , the contact front (the boundary between the driver and the driven gases) follows the shock wave; the resulting measurement is then recorded on the PXI.

$$U_b = U_1 - U_2 \quad (\text{Equation 120})$$



The Rankine-Hugoniot Equations¹ explain the fluid conditions in both the upstream and downstream regions of a shocktube [14].



¹ See Appendix A2

5.4: RESULTS, PLOTS AND TABLES

This section highlights the results from the experiment. The graphs are presented in the order of lowest and highest Mylar® membrane thickness. The membrane thickness determines the breech pressure, and the intensity of each blast wave.

The graphs are the observation made during the experiment and explained in the discussions section below.

Breech	Barrel	End Config.	Breech sensor range (psi)	Breech Length (in)	Membrane Thickness (in)	Driver Gas	Temperature (F)	Baro. Pressure (kPa)	Relative Humidity (%)	Burst Pressure (psi)
4" Dia.	9" Sq.	Head	500	11.625	1x0.01	Nitrogen	74.06	983.73	29.6	91.51
4" Dia.	9" Sq.	Head	500	11.625	3x0.01	Nitrogen	74.13	983.9	28.56	314.05
4" Dia.	9" Sq.	Head	500	11.625	5x0.010	Nitrogen	74.79	985.5	28.49	528.36
4" Dia.	9" Sq.	Head	500	11.625	5x0.01	Nitrogen	74.42	984.42	26.4	501.55
4" Dia.	9" Sq.	Head	1000	11.625	5x0.01	Nitrogen	74.86	984.01	25.53	545.72
4" Dia.	9" Sq.	Head	1000	11.625	5x0.01	Nitrogen	74.51	983.98	25.07	600.48
4" Dia.	9" Sq.	Head	1000	11.625	5x0.01	Nitrogen	74.45	983.91	24.48	590.84
4" Dia.	9" Sq.	Head	1000	11.625	7x0.01	Nitrogen	74.67	984.61	24.72	835.82
4" Dia.	9" Sq.	Head	1000	11.625	8x0.01	Nitrogen	74.38	984.47	24.58	965.57
4" Dia.	9" Sq.	Head	3000	11.625	10x0.01	Nitrogen	75.23	983.84	25.33	1212.67
4" Dia.	9" Sq.	Head	3000	11.625	10x0.01	Nitrogen	74.9	983.9	25.1	1218.73

Table 5.4.1: Shock Tube configuration results

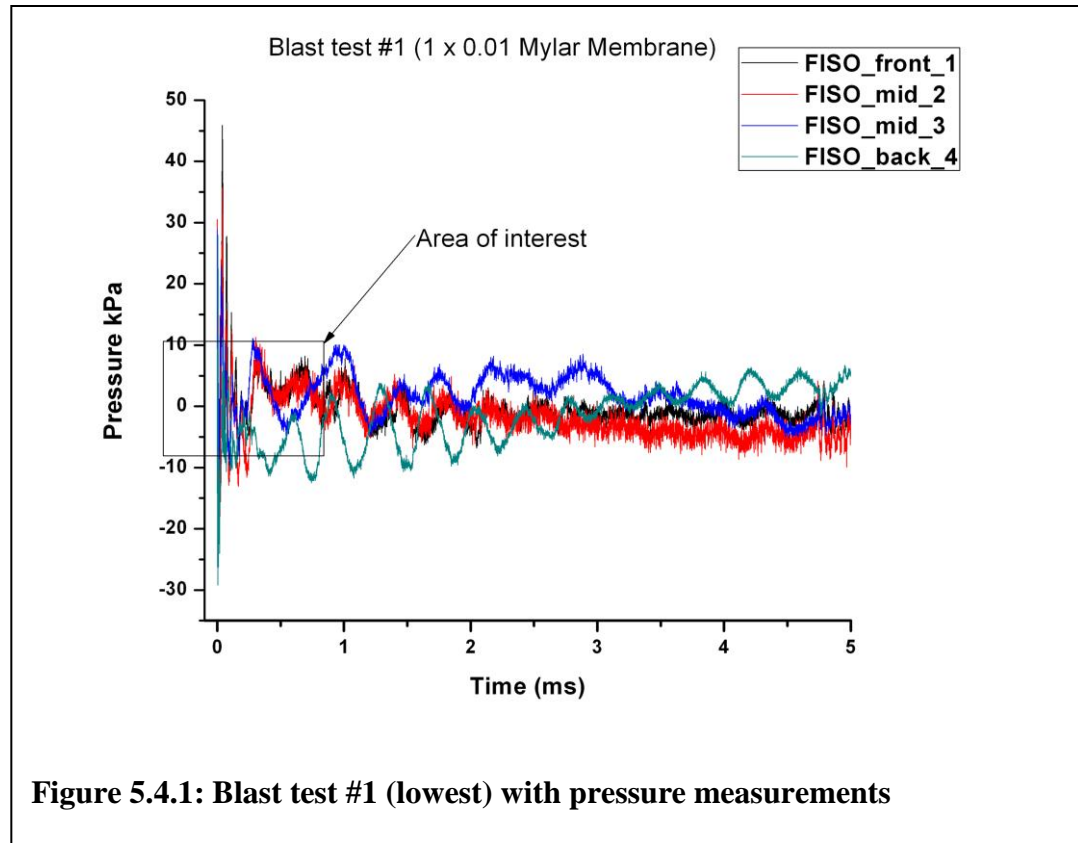


Figure 5.4.1: Blast test #1 (lowest) with pressure measurements

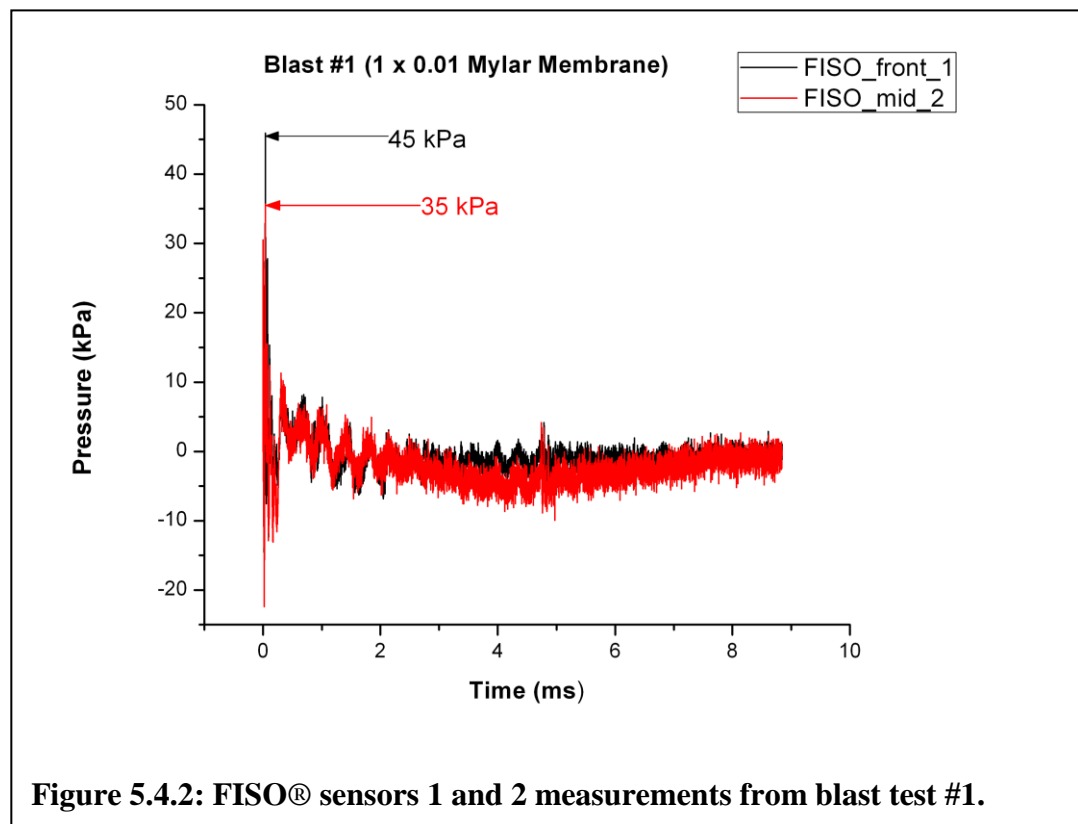


Figure 5.4.2: FISO® sensors 1 and 2 measurements from blast test #1.

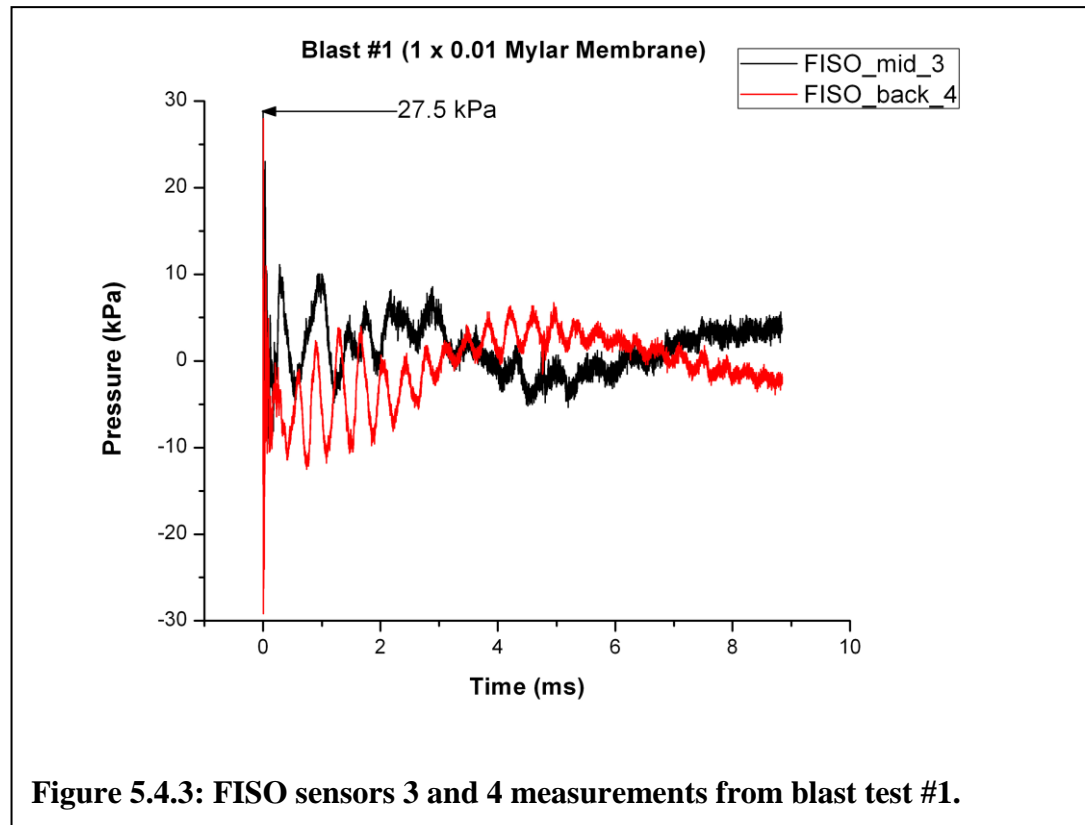


Figure 5.4.3: FISO sensors 3 and 4 measurements from blast test #1.

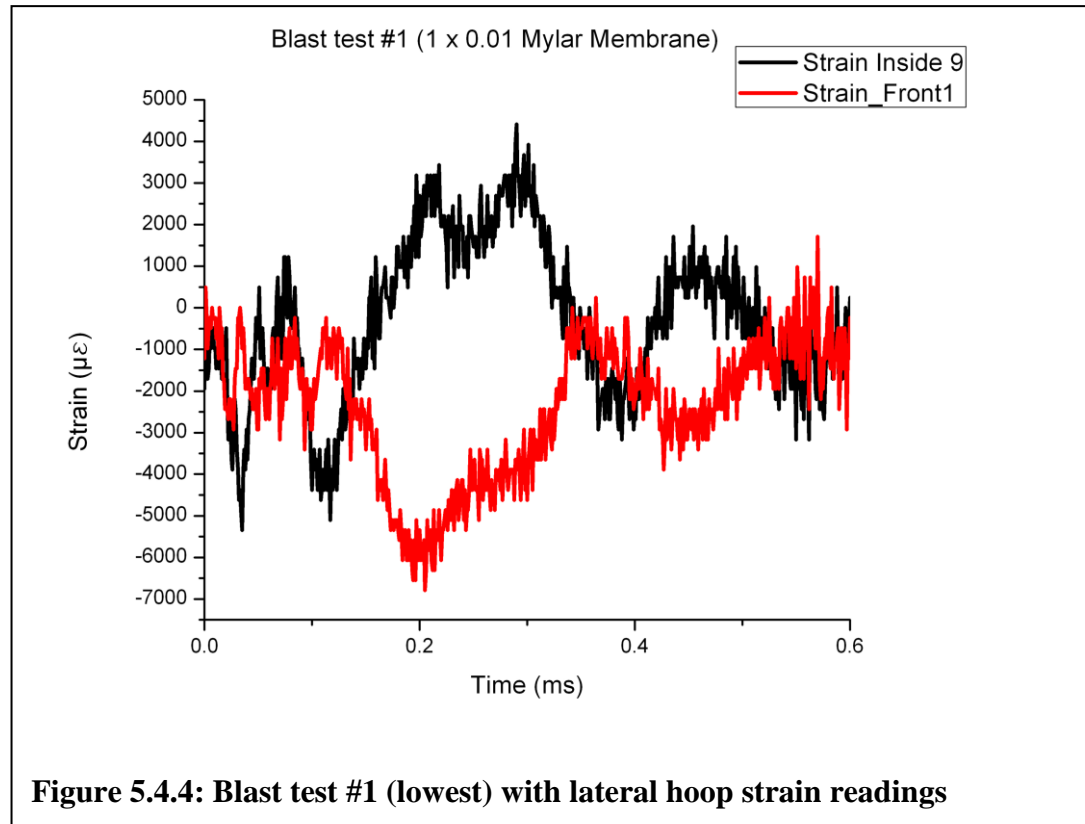
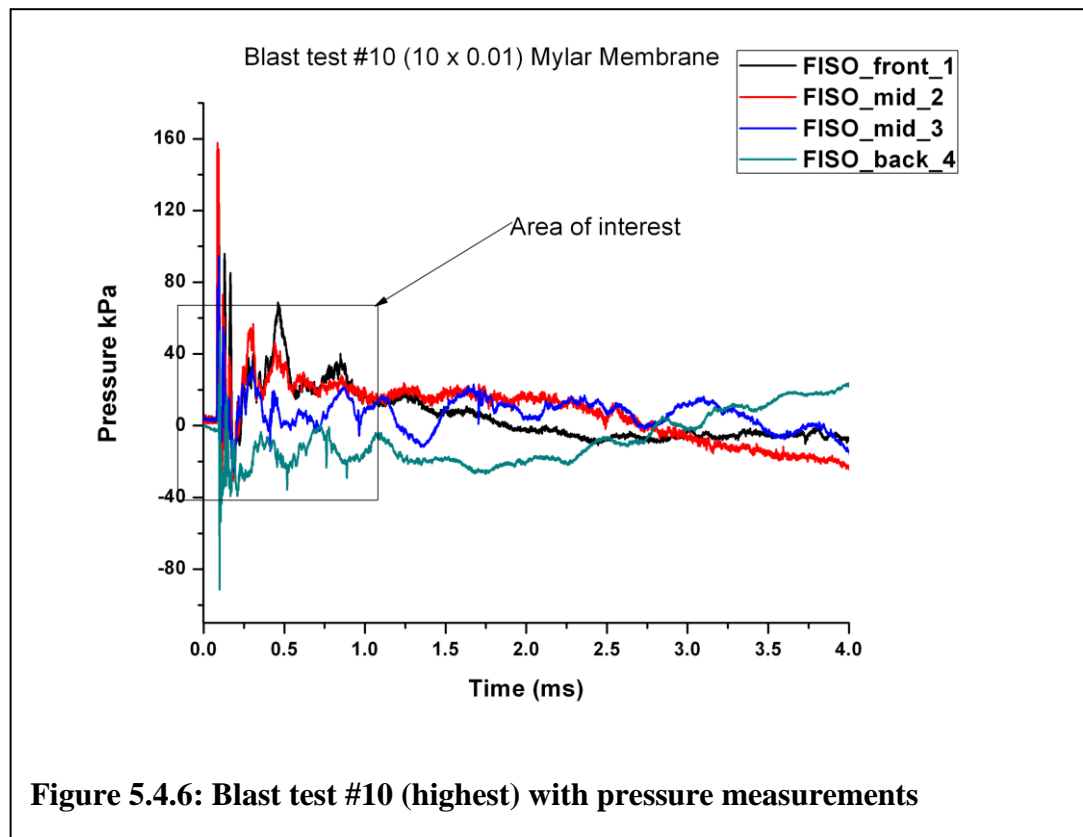
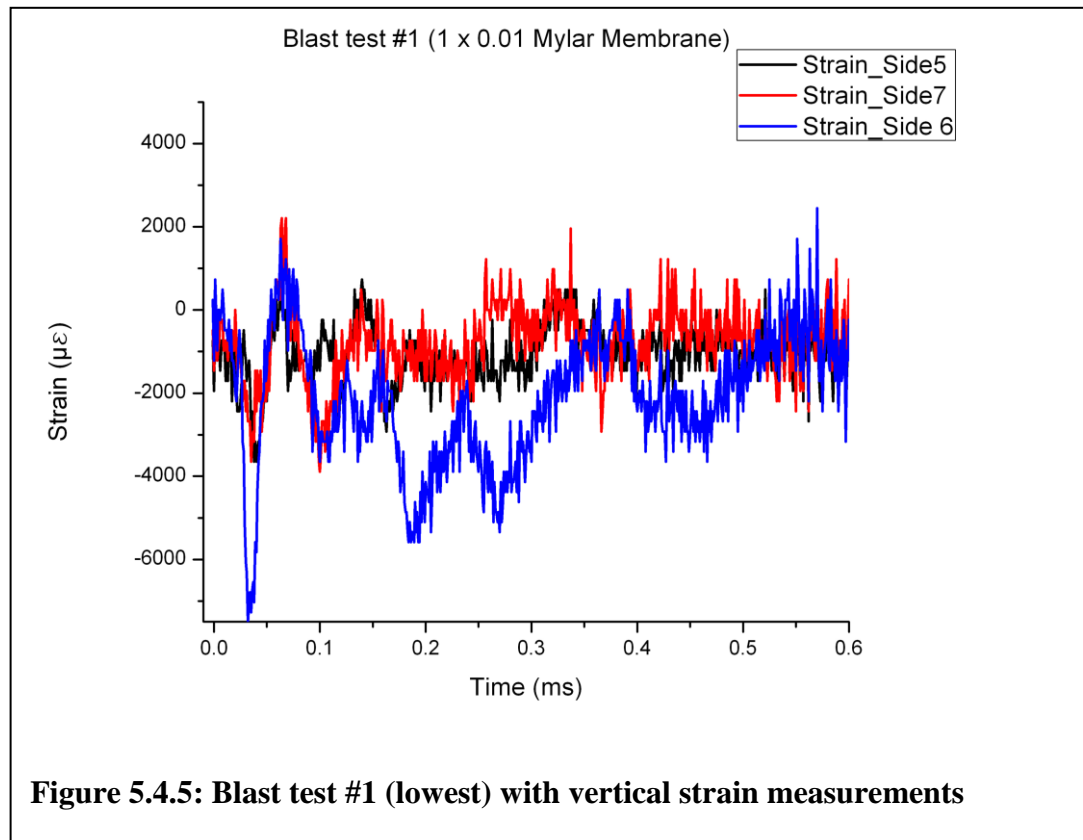
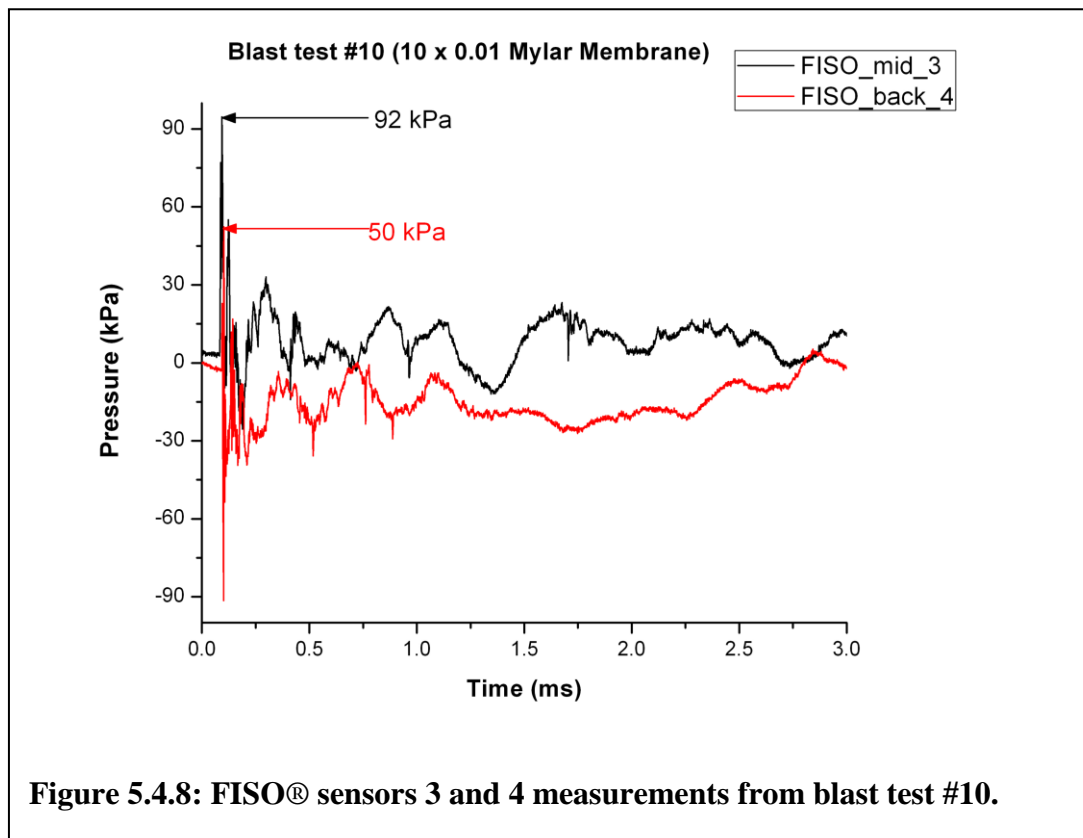
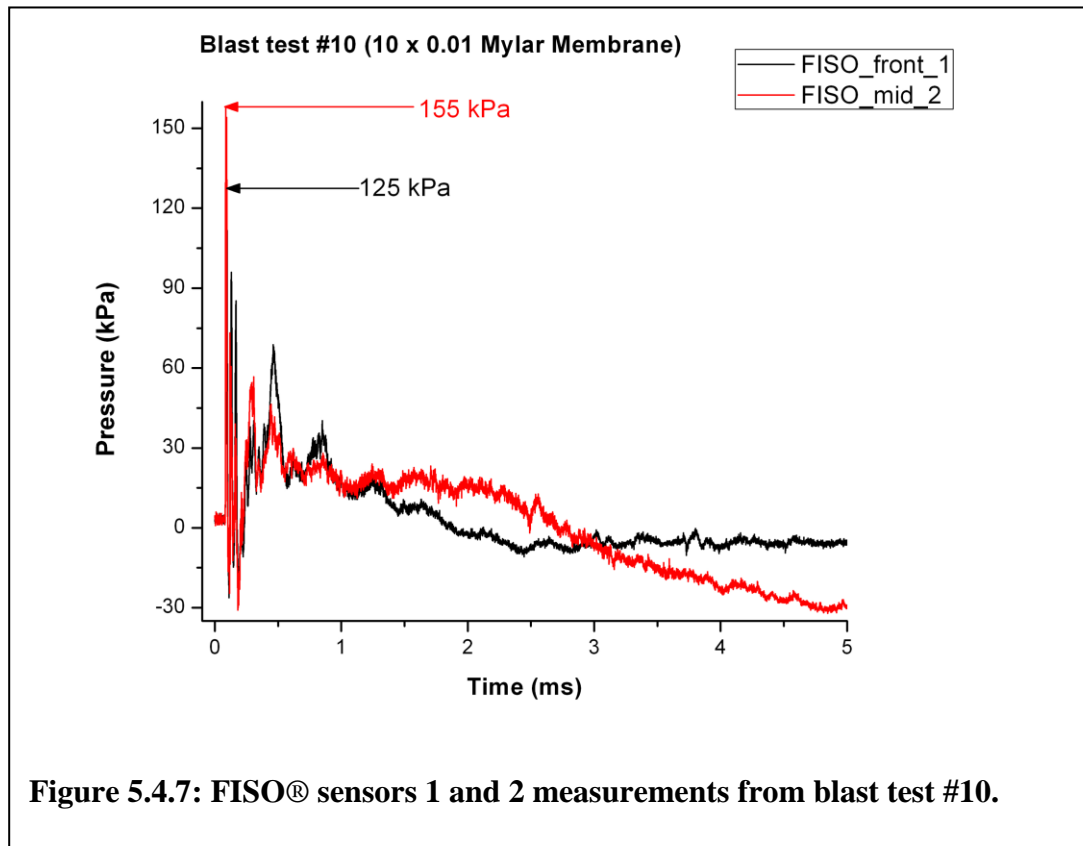


Figure 5.4.4: Blast test #1 (lowest) with lateral hoop strain readings





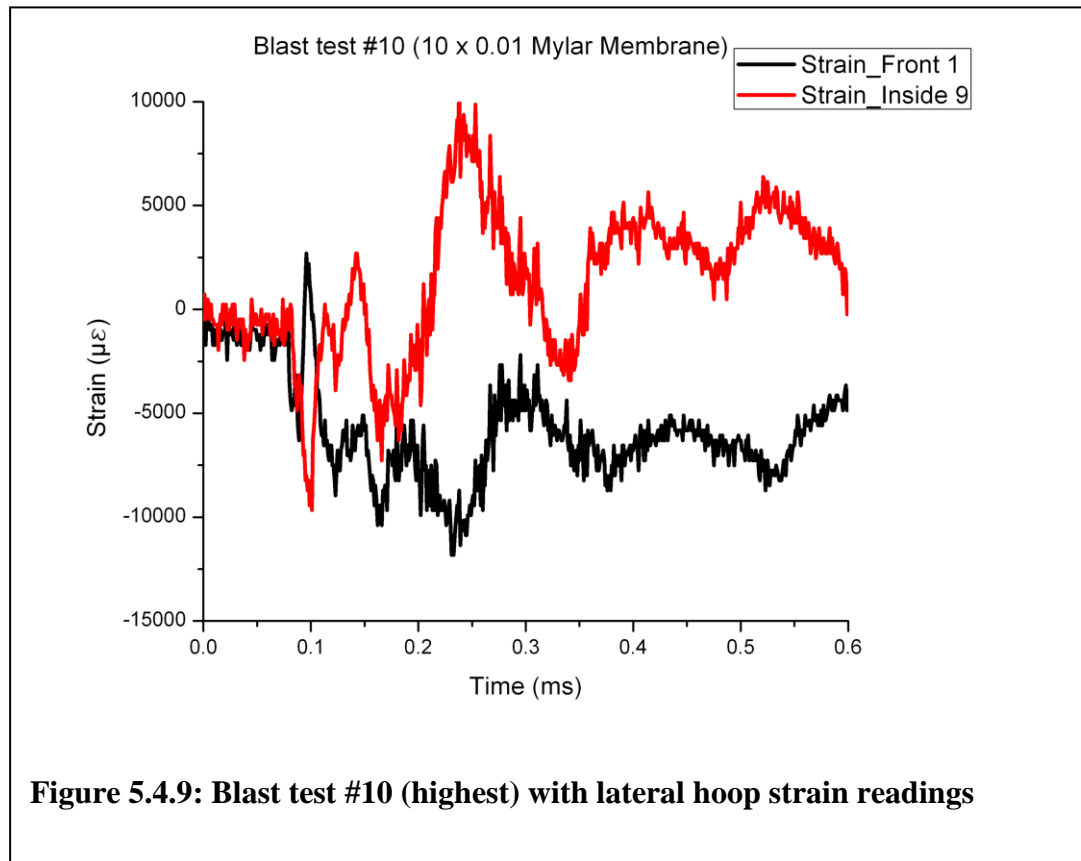


Figure 5.4.9: Blast test #10 (highest) with lateral hoop strain readings

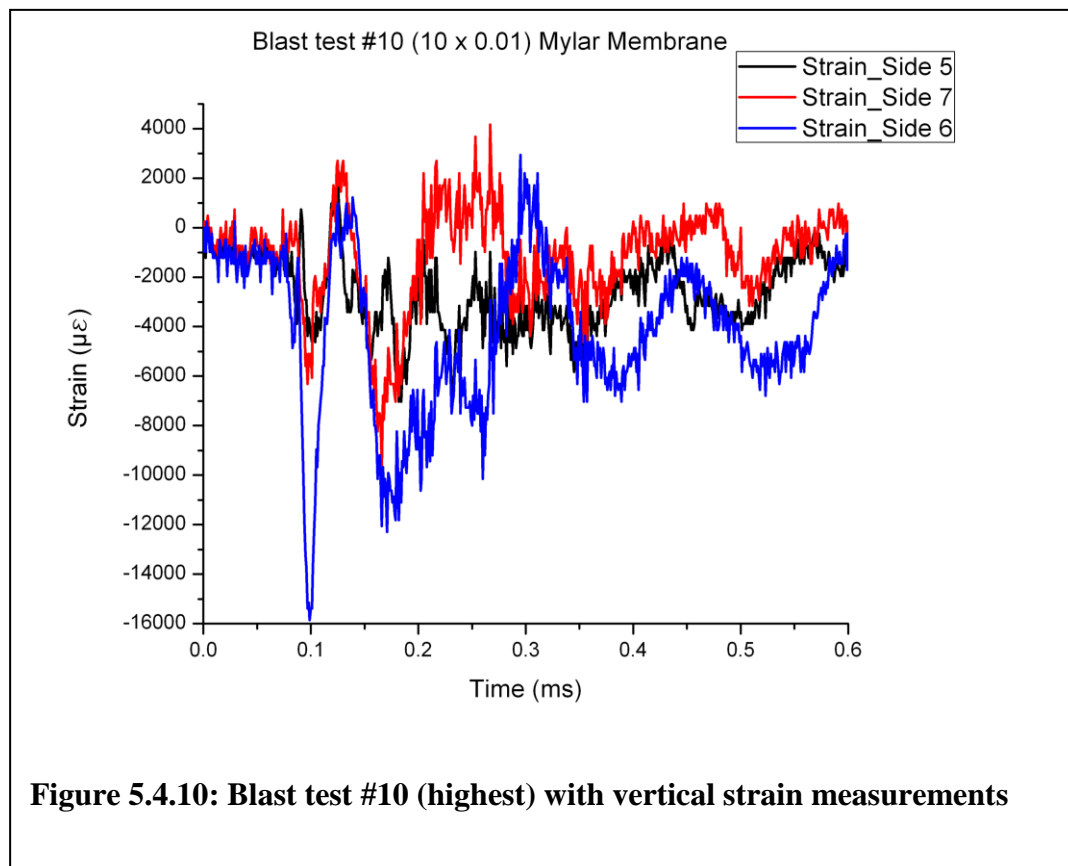


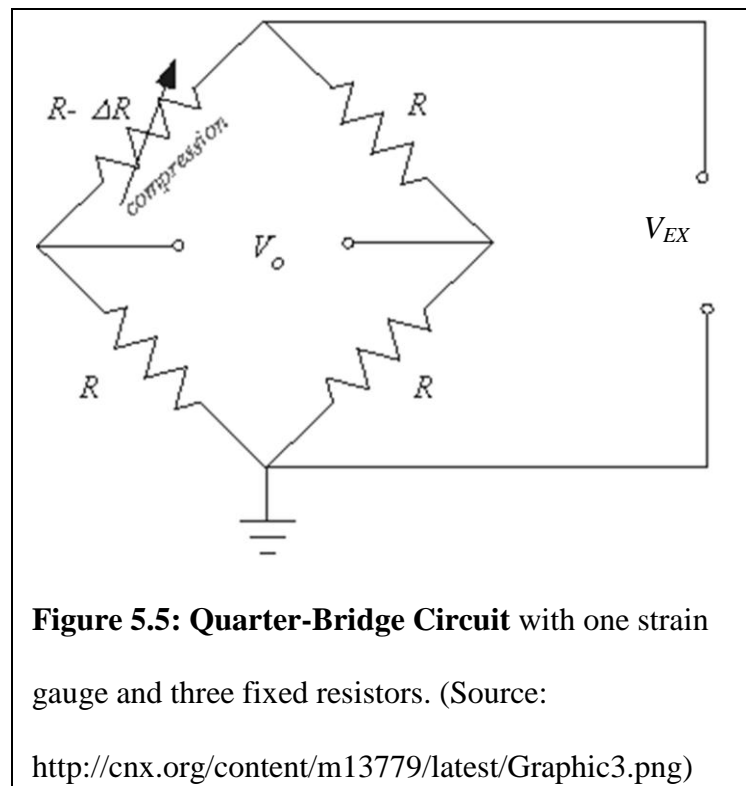
Figure 5.4.10: Blast test #10 (highest) with vertical strain measurements

5.5: DISCUSSIONS

Figures 5.4.1 to 5.4.4 shows the lowest blast level of breech pressures available using 1 by 0.01 Mylar® membrane from the experiment at 91.5 psi, while Figures 5.4.5 to 5.4.9 shows the highest blast level of breech pressure using 10 by 0.01 Mylar® membranes available at over 1200 psi.

From blast test # 1, the peak pressures for the FISO® sensors were noticed at 0.039 ms with sensor # 1 at 45.91 kPa, sensor #2 at 35.66 and sensor #3 at 17.71 kPa. The highest peak for sensor #4 was not noticed until 0.048 ms at 10.93 kPa.

From blast test # 10, the peak pressures for the FISO® sensors were noticed at 0.093 ms with sensor # 1 at 130.71 kPa, sensor #2 at 154.15 and 52.32 kPa.



The strain measurements from the plots have been converted from voltage to micro-strain ($\mu\epsilon$) for clarity.

For the conversion, the quarter bridge equations were used to derive a formula for the value of strain:

$$V_O = \left[\frac{R_3}{R_3+R_4} - \frac{R_3}{R_1+R_2} \right] \cdot V_{EX} \quad (\text{Equation 21})$$

$$V_O = \left[\frac{R_3}{R_3+(R_4+\Delta R)} \right] \cdot V_{EX} \quad (\text{Equation 22})$$

$$V_O = \left[\frac{R}{R-\Delta R+R} - \frac{R}{R+R} \right] V_{EX} \quad (\text{Equation 23})$$

$$\frac{V_O}{V_{EX}} = -\frac{G_F}{4} \epsilon \left(\frac{1}{1+G_F \frac{\epsilon}{2}} \right) \quad (\text{Equation 24})$$

$$\frac{\epsilon}{1+G_F \frac{\epsilon}{2}} = -\frac{4V_O}{V_{EX}G_F} \quad (\text{Equation 25})$$

Let

$$X = \frac{4V_O}{V_{EX}G_F} \quad (\text{Equation 26})$$

$$\epsilon = -X \left(1 + G_F \frac{\epsilon}{2} \right) \quad (\text{Equation 27})$$

$$\epsilon = \frac{-X}{1+\frac{G_F}{2}X} \quad (\text{Equation 28})$$

Substituting Equation 26 back into Equation 28,

$$\varepsilon = \frac{-4 V_o}{V_{EX}G_F+2G_FV_o} \quad (\text{Equation 29})$$

where, ε = strain

V_o = Output voltage

V_{EX} = Excitation voltage

G_F = Gauge factor

ΔR = Resistance change

$R = R_1, R_2, R_3$ = Fixed resistors

R_4 = Strain gauge

With a gauge factor of 2 and an excitation voltage of 5V we can find the change in R, using the strain gauge resistance value of 350 Ohms.

The strain measurement from blast test #1 increased significantly on blast test # 10, measuring peak to peak there was an increase of $5000\mu\varepsilon$, pressure measurements from both blast #1 and #10 shows a sharp rise with a full pressure peak profile due to the shock wave and then a trailing edge decline in the amplitude due from the expansion waves.

Lateral hoop strain measurement on the skull of the RED Head shows a deflection in the inside strain gauge #9 when compared to front outside strain gauge #1, even on both blast tests #1 and #10. The vertical strain measurement, when compared in both tests shows lots of strain activity as the wave propagates through the RED Head with strain gauge #6 with the highest peak of $-1600 \mu\epsilon$, followed by strain gauges #5 and #7.

Examining the data set thoroughly reveals that FISO® sensor #4 shows a sharp decline at the same time domain when the other sensors are experiencing an increase in amplitude (see Table 5.6.1 and 5.6.3).

The jump noticed in FISO® sensor #2 in blast test #10 could be as a result of a diffraction effect. This phenomenon occurs when there is a bending in the wave as a result of an obstacle or an interference with a refracted wave.

In terms of the order of amplitudes, all the blast tests follows the same pattern, but with different peak pressure. There was some sort of delay for strain gauge #1 as it rises and falls very quickly and remained at par with strain gauge #5 while its amplitude decreases due to interference to indicate a zero displacement.

From Figure 5.4.2 the baseline noise for the FISO® sensors is estimated to be about 5 kPa and the corresponding peak stands at about 45 kPa; therefore the signal to noise ratio is approximately 9. The noise level in other measurements using the same hardware settings is not expected to differ significantly from this baseline value. For the strain gauges, the baseline noise is estimated to be about $2000 \mu\epsilon$ as shown in Figure 5.4.5.

The readings from the sensors can be attributed to the planar shock wave and the refracted shockwave being out of phase, in some cases, allowing the wave crests to align with the wave troughs, as it propagates through the RED Head and into the surrogate brain. The normal shock as it moves from the origin becomes oblique as it touches the RED Head and began to refract into the silicone gel, and the wave will focus around the center of the gel such as *light* will in an optical convergence, and in essence cause more pressure build-up.

It should be noted that the intensity of the wave form in the direction of the shock as it propagates in the shock direction was consistent in both the FISO® pressure sensors and strain gauge readings. Therefore at a distance r from the membrane, the power P of the shock passes through an area $4\pi r^2$ - the surface area of the RED Head with radius r .

$$I = P/A = P/ 4\pi r^2 \quad (\text{Equation 30})$$

The intensity of the pressure blast, an exponential function of the path length, gradually depletes as it propagates from the membrane source to the RED Head. As the shock wave propagates towards the RED Head, the inside strain gauge records the bending due to the shock front as it moves along the shock path, sending the head into a backward jolt, and there is a reflection of the shock wave towards the source, and the shock front diffracted around the RED Head, allowing a gradual permeation into the skull and ultimately the brain, and a large pressure build-up inside the RED Head as noticed in the measurements.

The tests should normally show a gradual decrease of the amplitude as it propagates towards the back, but a pressure build-up near the middle of the brain.

Blast waves from the shock tube are estimated to travel at several hundred m/s. Wave speed in the surrogate brain can be determined by the gel's compressibility and density. Since waves in solids propagate longitudinally and transversely, one can approximately predict the wave speed of longitudinal waves moving through the skull simulant and into the brain simulant medium, as well as shear waves which may propagate around the skull from front to back [50].

Chapter 6: Conclusions

6.1: CONCLUSIONS

Traumatic brain injury (TBI) as a result of improvised explosive devices (IED) is on the rise in the military, and improved understanding of the phenomena involved would lead to new advances in soldier safety. That is why this research was undertaken. The aim of this research is to select the most optimal instrument and sensors to understand the effects of blast waves on the head. This requires some knowledge of basic principles of these instruments and a broader knowledge in general about what to measure and how to accomplish the measurements.

The long-term goal is to determine how shockwaves attenuate as they propagate into the head and in particular the brain. This thesis has taken a step forward in designing instrumentation for a surrogate headform and brain simulant that has similar mechanical properties as those found in a human head. Some of the best instruments and sensors in the industry today were selected to enable us to determine pressure variations and other phenomena in the headform.

The work involved the design of the RED Head, including material selection for the tissue surrogates, and focusing especially on instrument and sensors selection and design, calibration of the data acquisition system, experiment design and data analysis.

Calibrating the instruments enabled us to understand how each of the sensors behaves. Limitations on the time duration in which the FISO® sensor gives reliable data were determined. We were also able to determine bounds on the noise level of each

sensor, their limitations and characteristics. Having a good understanding of their behavior will lessen the effort needed to re-calibrate and will serve as a valuable information resource for continuing with this research.

A Matlab® code for post-processing was generated to handle the large amount of data obtained in shocktube experiments. The LabVIEW® code and interfaces between the data acquisition system to read, write and store the data was also generated.

The sensors and strain gauges were fitted on the RED Head appropriately to obtain the desired measurements; all design work and calibration were carried out with adherence to accepted practices. The set-up and operation of the shocktube was done with safety in mind. Instrumenting the headform with fiber optic sensors and strain gauges enables determination of the pressure profiles experienced in the RED Head.

The results show that there is significant pressure buildup in the human brain, centered near the middle, and that the shockwave, though planar at the time of impact becomes non-planar at the time of entry and propagation into the skull. The shockwave develops into a uniform profile as it travels from the burst location downstream toward the headform, and its amplitude decreases as it travels through the headform due to energy dissipation. Significant damage can be done within a few milliseconds, even if unnoticed to the observer.

6.2: FUTURE WORK

There are a number of ways in which the RED Head could be improved and these are discussed as follows.

The PDMS skin should be completely laminated to the skull in future experiments and the eye cavity filled with a similar surrogate. This would improve fidelity by avoiding skin delamination and accounting for more feature detail.

The RED Head experiences complex stimuli including acceleration effects, wave dispersion and scattering; the experiments should be refined in the future to account for more of these factors, for example, by adding more pressure sensors strategically throughout the surrogate brain to detect the pressure variation present and by including accelerometers on the skull surface. Results captured with high-speed cameras could also be used to correlate accelerometer and strain gauge measurements.

More precise positioning of the FISO® sensors would enable us to understand the wave speed in the gel medium. Future work should accommodate this. A probe sensor on the front of the RED Head could also be employed to identify the amplitude of the incident wave hitting the head.

Effectively simulating the CSF with water or other fluid media would improve fidelity with respect to interface effects (scattering, reflection etc.). To avoid cavitation issues, distilled water could be used as it eliminates impurities (dissolved gases).

A shock tube bigger than the current 9" square barrel needs to be used for future tests, as it would allow the RED Head to be placed inside the tube and along the path of the shockwave rather than outside the path of the uniform shock wave where the pressure profile is more difficult to ascertain.

Future experiments may also explore the effects of target geometry. The effects of oblique blast wave around a spherical object could be investigated to determine the characteristics of this wave pattern as it propagates.

Geometry is also thought to be important for shock effects on protective equipment. Current Kevlar® helmets are good ballistic protective devices but not against blast wave threats. New kinds of head protection system that are able to offer protection not just to the upper part of the skull but the entire head and are able to prevent or diminish penetration of the blast wave should be developed.

The work presented in this thesis represents a significant step forward in the pursuit of the long-term research goals and may eventually lead to technological developments relevant to soldier protection.

Works Cited

1. **Phillips Y. Y.** Primary Blast Injuries. *Ann Emerg Med.* 15:1446-50, 1986.
2. **Chavko, M., Koller, W. A., Prusaczyk, W. K., and McCarron, R. M.** Measurement of blast wave by a miniature fiber optic pressure transducer in the rat brain. *Journal Of Neuroscience Methods.* 2007, Vol. 159, 227-281.
3. **Lawrence Livermore National Laboratory.** Traumatic Brain Injury. *S&TR* . March 2010.
4. **Miles, Donna.** AFIS: News Articles. *www.globalsecurity.org.* [Online] January 7, 2008. [Cited: October 20, 2010.]
<http://www.globalsecurity.org/military/library/news/2008/01/mil-080107-afps08.htm>.
5. **Strich, S. J.** *Shearing of nerve fibres as a cause of brain damage due to head injury: a pathological study of twenty cases.* London : s.n., 1961. OCLC: 603454539.
6. **University of Toronto.** Workshop on Brain Biomechanics. *Presentation Notes.* Toronto, Canada : Centre for Mathematical Medicine, 2007.
7. **University of Nebraska-Lincoln.** Basics of Blast Physics, Damage and Injury. *Presentation Notes.* Lincoln : Dyn-FX Consulting Ltd, July 2009.
8. **Langlois, J. A., Rutland-Brown, W., and Thomas, K. E.** *Traumatic brain injury in the United States: Emergency department visits, hospitalizations, and deaths.* Atlanta

(GA) : Centers for Disease Control and Prevention, National Center for Injury Prevention and Control, 2006. http://www.cdc.gov/traumaticbraininjury/pdf/blue_book.pdf.

9. **Ylvisaker, M., et al.** Educating students with TBI: Themes and Recommendations.

Journal of Head Trauma Rehabilitation. 2001, Vol. 16, Issue 1, pp. 76-93.

10. **National Institute of Neurological Disorders and Stroke.** *Traumatic Brain Injury:*

Hope Through Research - A Brochure. Bethesda, Maryland, USA : National Institute for Health, February 2002.

11. **Bronzino, J. D.** *The Biomedical Engineering Handbook.* s.l. : CRC Press, 2000.

ISBN: 0849321247.

12. **Defense and Veterans Brain Injury Center (DVBIC).** *[unpublished].* Washington

(DC) : U.S. Department of Defense, 2005.

13. **Bochicchio et al.** *Blast Injury in a Civilian Trauma Setting Is Associated with a*

Delay in Diagnosis of Traumatic Brain Injury. THE AMERICAN SURGEON. March

2008, Vol. 74, 3, p. 267-270.

14. **Kinsler, L. E., Frey, A. R., Coppens, A. N., and Sanders, J. V.** *Fundamentals of*

Acoustics. New York : John Wiley and Sons, Inc, 2000. ISBN: 0471847895.

15. **White, F. M.** *Fluid Mechanics.* New York : McGraw-Hill Higher Education, 2011.

ISBN-10 0-07-352934-6.

16. **Su, Z., et al.** *Experimental investigation of a novel blast wave mitigation device*. s.l. : Shock and Vibration 16, 2009. DOI 10.3233/SAV-2009-0487.
17. **Wikipedia.** Combat Helmet. *Wikipedia.org*. [Online] November 14, 2010. [Cited: November 15, 2010.] http://en.wikipedia.org/wiki/Combat_helmet.
18. **Hsieh, A. J., Orlicki, J. A., and Beyer, R. L.** *Molecular Design of Novel Poly(urethane-urea) Hybrids as Helmet Pads for Ballistic and Blast Trauma Mitigation*. Aberdeen Proving Ground, MD : Army Research Laboratory, March 2009. ARL-TR-4764.
19. **Mott, D. R., Schwer, D. A., Young, T. R. Jr., Levine, J., Dionne, J., Makris, A., and Hubler, G.** Blast-Induced Pressure Fields Beneath A Military Helmet. *American Physical Society*. BAPS.2008.DFD.MF.8, 2008.
20. **Ponce E. L., and Ponce D. S.** *Two Dimensional Finite Element Analysis for the Effect of a Pressure Wave in the Human Brain*. London, UK : International Electronic Conference on Computer Science 2007, 2007. ISBN: 978-0-7354-0590-5.
21. **Hossain, S. G. M., Nelson, C. A., Sogbesan, E., Boulet, T., Arnoult, M., Zhang, L., Holmberg, A., Hein, J., Kleinschmit, N.** *Material Modeling and Development of a Realistic Dummy Head for Testing Blast Induced Traumatic Brain Injury*. Paris, France : IV European Conference on Computational Mechanics, Palais des Congrès, May 16-21, 2010.

22. Advisory Group for Aerospace Research and Development/NATO.

Anthropomorphic Dummies for Crash and Escape System Testing. Quebec, Canada : AGARD, 1996. ISBN-92-836-1039-3.

23. Anctil, B.; Wonnacott, M.; and Sullivan, D. *Preliminary Study of the Effects of*

Combat Helmet on Head/Neck Response under Rear/Side Impacts. Valcartier, Quebec : Defence Research & Development Canada, 2009. DRDC-VALCARTIER-CR-2008-392.

24. Bourget, D., Anctil, B., Doman, D., Cronin, D., Development of a Surrogate

Thorax. *Personal Armour Systems Symposium.* The Hague, The Netherlands : PASS, 2002. pp. 69-78.

25. Fournier, E., Sullivan, D., Bayne, T., and Shewchenko, N. *Blast Headform*

Development - Literature Review. Quebec, Canada : DRDC Valcartier, 2007. DRDC Valcartier CR 2007-234.

26. Hossain, S. G. M. *Material Modeling and Analysis for the Development of a*

Realistic Blast Headform - MS thesis. Lincoln, Nebraska : University of Nebraska-Lincoln, 2010.

27. Cohen, B., Voorhees, A., Vedel, S., and Wei, T. Development of a theoretical

framework for analyzing cerebrospinal fluid dynamics. *Cerebrospinal Fluid Research.* 2009, Vols. doi:10.1186/1743-8454-6-12.

28. Fishman, R.A. *Cerebrospinal Fluid in Disease of the Nervous System.* Philadelphia :

Saunders, 1980.

29. **Taylor, P. A., and Ford, C. C.** *Modeling and Simulation of Blast Induced, Early-Time Intracranial Wave Physics Leading to Traumatic Brain Injury*. Livermore, California : Sandia National Laboratory, 2008. doi:10.1115/1.3118765.
30. **Hill, C.** *Simplifying the instrument selection process in a hardware independent environment*. Anaheim, CA , USA : AUTOTESTCON, 97. 1997 IEEE Autotestcon Proceedings, 22 Sep 1997 - 25 Sep 1997. ISBN: 0-7803-4162-7.
31. **Kawai, H.** *The piezoelectricity of polyvinylidene fluoride*. s.l. : Jap. J. Appl.Phys.,8:pp. 975-976, 1969.
32. **Odon, A.** Probe with PVDF Sensor for Energy Measurements of Optical Radiation. *MEASUREMENT SCIENCE REVIEW*,. 2003. Vol. 3, Section 3.
33. **Ueberschlag, P.** *PVDF PIEZOELECTRIC POLYMER*. Saint Louis, France : PIEZOTECH S.A./MCB University Press, 2001. ISSN 0260-2288.
34. **Sogbesan, E.** *Design and Analysis of Data Acquisition System of Realistic Dummy (RED) Head in a Shockwave Environment - Seminar Presentation*. Lincoln : University of Nebraska, 2010.
35. **Window, A.L. (Ed.)**. *Strain Gauge Technology; 2nd edition*. New York : Springer, 1993. ISBN: 978-1-85166-864-9.
36. **Vishay Micro-Measurements**. MR-Series Bridge Completion Modules - Product datasheet. *www.micro-measurements.com*. [Online] January 27, 2010. [Cited: 11 06, 2010.] <http://www.vishaypg.com/docs/11042/mrseries.pdf>. Document Number: 11042.

37. **Einstein, A.** *Relativity: The Special and General Theory*. New York : Henry Holt, 1920. ISBN 1-58734-092-5.
38. **Books LLC (Editor).** *Accelerometers: Accelerometer, Piezoelectric Accelerometer, Piga Accelerometer, Gravimeter, Liquid Capacitive Inclonometers*. s.l. : Books LLC, 2010. ISBN-13: 978-1156318584.
39. **Agarwal, A., Lang, J. H.** *Foundations of analog and digital electronic circuits*. San Fransisco : Elsevier, 2005. ISBN: 978-1558607354.
40. **Honeywell International Inc.** Test & Measurement. *www.honeywell.com*. [Online] 2008. [Cited: October 26, 2010.]
http://content.honeywell.com/sensing/sensotec/accelerometer_faq.asp?category=All.
41. **FISO Technologies, Inc.** Veloce 50 Signal Conditioner - Operating Manual. Quebec, Canada : s.n., 2004. DOC: MAN-00029R7.
42. **Lú, T., Li, Z., Xia, D., He, K., and Zhang, G.** Asymmetric Fabry–Pérot fiber-optic pressure sensor for liquid-level measurement. *REVIEW OF SCIENTIFIC INSTRUMENTS*. 80, 2009, Vol. 033104.
43. **Hernandez, G.** *Fabry–Pérot Interferometers*. Cambridge : Cambridge University Press, 1986. ISBN: 0521322383.
44. **National Instruments, Inc.** What Is PXI? *www.ni.com*. [Online] October 6, 2010. [Cited: October 29, 2010.] <http://zone.ni.com/devzone/cda/tut/p/id/4811>.

45. **Kester, W.** What the Nyquist Criterion Means to Your Sampled Data System Design. *Analog.com*. [Online] 2009. [Cited: November 22, 2010.]
<http://www.analog.com/static/imported-files/tutorials/MT-002.pdf>. MT-002.
46. **Dahlberg, G.** Materials Testing Machines Investigation of error sources and determination of measurement uncertainty. *EUROLAB International Workshop: Investigation and Verification of Materials Testing Machines*. [Online] [Cited: November 12, 2010.] http://www.mts.com/downloads/3_eurolab_dahlberg.pdf.
47. **Morris, A. S.** *Measurement and Calibration Requirements for Quality Assurance to ISO 9000*. West Sussex, England : Wiley, 1998. ISBN: 978-0471976851.
48. **Ganpule, S., Cao, G., Gu, L., and Chandras, N.** The Effect of Shock Wave on A Human Head. *2009 ASME International Mechanical Engineering Congress and Exposition*. Lake Buena Vista, Florida : Proceedings of IMECE2009, November 13-19, 2009. IMECE2009-12875.
49. **Ganpule, S.** *Shock Tube Blast Test Modeling and Validation*. Lincoln : Unpublished, 2010.
50. **Davison, L.** *Fundamentals of Shock Wave Propagation in Solids*. Tijeras, New Mexico : Springer, 2008. ISBN: 978-3-540-74568-6.

Appendix

A1: Matlab® CODES

```

load 'E:\FIZO3\FIZO1004.txt'
load 'E:\Strain.txt'
x=FIZO1004(:,1);
y=FIZO1004(:,2);
x1=Strain(:,1)
y2=Strain(:,2)
plot(x,y);
Offset=-0.0564;
ScaleFactor= 0.030006*10^3;
result1= y*ScaleFactor + Offset;
result2= result1*6.895
plot(x1,y2)
End

```

```

load 'C:\Documents and Settings\temp\Desktop\fizo.txt'
load 'C:\Documents and Settings\temp\Desktop\output.txt'
xf=-0.0006634;
xop=-0.000447;
c=5000;
icr=fizo(2,2)-fizo(1,2)%Time increment
nsf=(xf-fizo(1,2))/icr+1;%number of points left out on fizo data
n=round(nsf)
fizo=fizo(n-c:end,1);%new fizo data increased by c number of data
that will be on the left side of the plot;
nso=(xop-output(1,2))/icr+1;%number of points left out on output
data
m=round(nso)
output=output(m-c:end,1);%new output data increased by d number
of data that will be on the left side of the plot
[li c]=size(fizo);
[lo co]=size(output);
tfz=-c*icr:icr:(li-c-1)*icr;
tout=-c*icr:icr:(lo-c-1)*icr;
plot(tfz,fizo,tout,output)
End

```

A2: RANKINE-HUGONIOT EQUATIONS

Assuming a one-dimensional steady flow through a fixed normal shock wave, passing from upstream (section 1) towards the downstream (section 2) as shown in Figure 5.3.4:

Continuity: $\rho_1 U_1 = \rho_2 U_2 = G = \text{constant}$

Momentum: $P_1 - P_2 = \rho_2 U_2^2 - \rho_1 U_1^2$

Energy: $h_1 + 1/2 U_1^2 = h_2 + 1/2 U_2^2 = h_0 = \text{constant}$

Perfect gas: $P_1/\rho_1 T_1 = P_2/\rho_2 T_2$

Constant C_p : $h = C_p T$; $k = \text{constant}$

where

$\rho = \text{fluid mass density, [kg/m}^3\text{]}$

$U = \text{fluid velocity, [m/s]}$

$P = \text{fluid pressure, [Pa]}$

$h = \text{specific enthalpy of the fluid}$